BIOPARTICLE CAPTURE AND SENSING UTILIZING NANOGRASS BASED MICROFLUIDIC DEVICES

BY

HENGKAN NI

THESIS

Submitted in partial fulfillment of the requirements
for the degree of Master of Science in Electrical and Computer Engineering
in the Graduate College of the
University of Illinois at Urbana-Champaign, 2012

Urbana, Illinois

Adviser:

Professor Rashid Bashir

ABSTRACT

For the past few decades, biosensors have been developed at a steady pace and played a crucial role in medical practices and many other biomedical applications. Upon performing a survey of desirable sensor properties such as low cost, high sensitivity, fabrication process, and time to result, a nanograss embedded microfluidic device emerged as a very attractive candidate for an electrochemical impedance spectroscopy (EIS) based biosensor. Such a sensing device is expected to perform direct sensing quickly with high sensitivity, and at low cost. In this work, the nanograss fabrication process is illustrated in detail. Then nanograss substrate itself is characterized by multiple approaches. In addition, COMSOL Multiphysics is used for finite element simulation of the flow through the microfluidic chamber. The EIS method is used to evaluate the capture and sensing ability of the fabricated nanograss embedded microfluidic device. The nanograss devices are shown to be able to capture and sense a few particles/μL, indicating that the nanograss devices could be used as next-generation biosensors.

To my lovely Janet and my parents for their everlasting love and support

ACKNOWLEDGMENTS

I am greatly obliged to my mentor, Prof. Rashid Bashir, for allowing me to become a part of his group and advising me throughout the process of this degree. I have learned a lot from him and would like to thank him for his valuable advice and words of encouragement. I could not have completed this project and degree without his guidance, help and support. I would also like to express my sincere gratitude to Dr. Nicholas Watkins. He has taught me some of the most important aspects of research and was always available to help me, even when he was extremely busy. I am extremely grateful to Gregory Damhorst and Umer Hassan for being with me on the same research team and helping me through the process of this degree.

I would like to thank Dr. Glennys Mensing, who gave me many useful suggestions for fabrication that were very important in this study. I am deeply thankful to all my group members for the invaluable discussions and support to carry out the work in the lab. In particular, I would like to thank Jose Rivera, Piyush Bajaj, Dr. Larry Millet, Caroline Cvetkovic, Katrina Keller, and Carlos Duarte.

Especially, I would like to thank Dr. Qiang Zou for so many years of good times and for valuable guidance and advice as my life mentor. I could never have come close to this without your help.

Finally and most importantly, I would like to thank my lovely Janet and my parents for their tremendous support all throughout my life and this work.

TABLE OF CONTENTS

CHAPTER 1. INTRODUCTION

1.1 Motivation and Purpose

Human immunodeficiency virus/acquired immunodeficiency syndrome (HIV/AIDS) is an infectious disease of the human immune system caused by HIV. In general, HIV roughly exists as spherical particles. An HIV particle is around 100-150 nm in diameter. On the other hand, HIV belongs to retroviruses, which means their genes are composed of RNA.

According to the World Health Organization (WHO) report, as shown in Fig. 1.1, the number of people living with HIV reached 34.2 million by the end of 2010. Among them, 2.5 million people were newly infected in 2010. During the same year, 1.8 million people died of AIDS. High prevalence and incidence of HIV/AIDS places a heavy burden on regional healthcare providers and has a severe influence on healthy sexually active individuals. Thanks to the previous efforts jointly made by scientists, engineers and doctors, the deadly HIV infection has become a manageable, though chronic, disease [1-2].

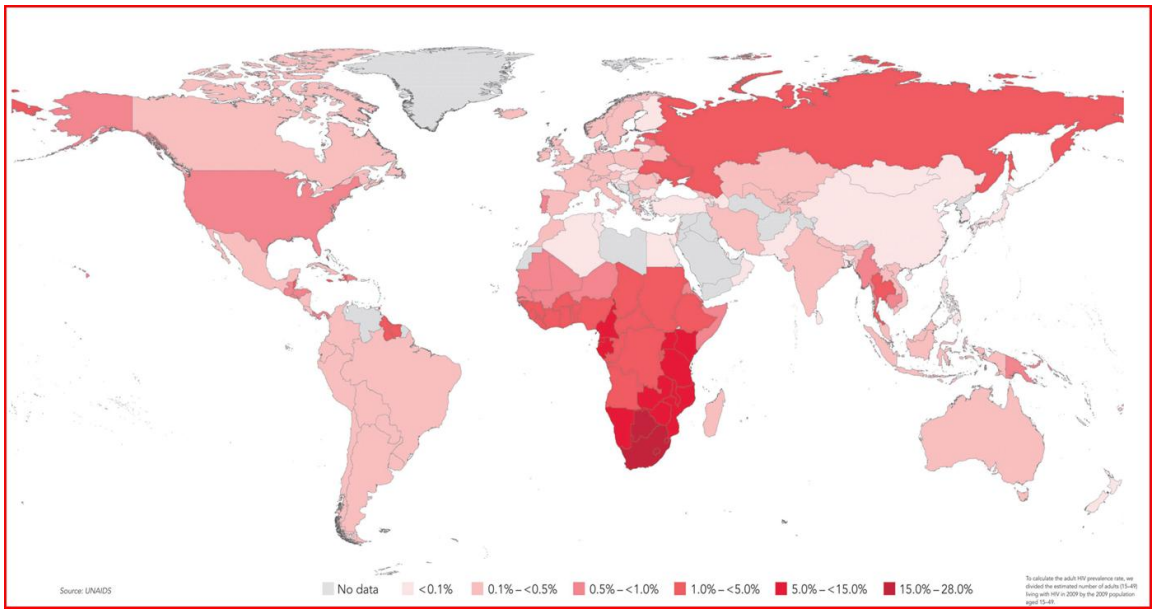

Fig. 1.1 HIV distribution around the world. Source: UNAIDS 2010.

To effectively monitor the health state of HIV positive patients, doctors measure viral load throughout the patient's life. It is tested soon after diagnosis with HIV infection and probably every 3-6 months after the first establishment of a baseline level. Because changes in viral load reflect the efficacy of medications or therapies, it is also tested before the beginning of a new HIV medication, and 2-8 weeks after starting or changing therapies. Sometimes, doctors may decide to start treatment based on viral load alone because of the strong association between increased viral load and increased destruction of CD4+ cells. A routine test in western countries, viral load testing is rarely practiced in other parts of the world due to cost and equipment requirement. Given its usefulness in monitoring and management of HIV positive patients, we have been working on the development of fast, portable, inexpensive devices in order to make the testing faster and more economical [3].

1.2 Current HIV/AIDS Monitoring

Before proposing our research plan, let us take a quick look at the current HIV/AIDS screening methods. First, patients are tested for the presence of the virus using a p-24 antigen or HIV antibody test. These are qualitative yes/no tests. If the patient has HIV, he or she would get a CD4+ T cell count to see whether he or she needs to start treatment. The viral load test can also be used to complement the CD4+ T cell count to provide more information regarding the patient's response to treatment.

We can also test for the p-24 protein to monitor HIV, as we know that the p-24 protein is part of the viral capsid. But the problem with this technology is that detecting with antibodies to the p-24 protein gives very low sensitivity (false negatives), and it is useful only for the first few weeks after infection. This is because the human body has already created antibodies to HIV during this period. For HIV test, usually western blot and ELISA (enzyme-linked immunosorbent assay) are recommended together, but neither of these is cheap, portable, or fast.

So, besides the CD4+ T cell counter, there is a huge need for a portable, robust, inexpensive method to bring a viral load test for AIDS diagnostics to resource-poor regions. In current medical practice, polymerase chain reaction (PCR) is employed to test viral load. PCR is a biochemical technology to amplify a single or a few copies of a piece of DNA across several orders of magnitude. Quantitative PCR methods allow the estimation of the amount of the initial DNA templates in blood sample. Since HIV is an RNA virus, variations of PCR, such as reverse transcription PCR (RT-PCR) and Nucleic Acid Sequence Based Amplification (NASBA), are used instead of original PCR. Apart

from PCR, Cavidi AB [4] developed ExzVir TM Load, which monitors viral load based on ELISA. It has been approved for clinical use.

Considering the cost and complexity of current medically used method, a direct detection of virus is highly desired. Therefore, electrochemical impedance spectroscopy (EIS) method is employed to investigate the changes of the electrode/electrolyte interface impedance when the virus is captured on-chip [5-7]. This method is to provide a basic understanding for current and potentially increasingly widespread virus sensing applications [8-10].

We propose a solution of using a bio-MEMS viral load sensor. Our goal with this device is to identify that the microchip electrical sensor can provide viral load test versus a western blot and ELISA. An EIS model is employed based on the concepts above. An impedance |Z| based sensor for virus is expected to: (a) capture virus; (b) measure |Z| vs. virus concentration.

1.3 Thesis Overview

The goals of this thesis are to evaluate the capture and sensing ability of a nanograss embedded microfluidic device and to evaluate nanograss as a biocompatible material for biosensors, which could be eventually developed into a point-of-care (POC) sensor for HIV viral load test. Chapter 2 will give a background and a thorough literature review about the fabrication of different impedimetric biosensors and their sensing ability. Chapter 3 will present the fabrication of nanograss and the preparation of

nanograss embedded devices for biomedical applications. Chapter 4 will focus on the characterization of nanograss devices, in terms of capture capability, surface hydrophobicity test, and surface enhanced Raman spectroscopy (SERS) effect. A brief discussion will follow these results. Chapter 5 will present a finite element simulation of the flow test. COMSOL Multiphysics is employed for this simulation. Chapter 6 will present the experimental data of bioparticle capture and sensing on a nanograss embedded microfluidic device. Chapter 7 will outline the conclusions that have been reached during the course of this work and also provide some recommendations for future work.

CHAPTER 2. BACKGROUND AND LITERATURE REVIEW

2.1 Introduction

The purpose of this chapter is to provide a starting point to understand the characteristics of different biosensors. This chapter will therefore provide the significance of the present study. Also, included in this chapter will be a discussion of the past work of other research groups' biosensors for medical applications. Section 2.2 will present the basic principles for a biosensor. Section 2.3 will discuss the point-of-care biosensors. Section 2.4 will then talk about the planar (2D) electrode biosensors. Section 2.5 will evaluate the recently developed hybrid-nanostructured (3D) biosensors. Section 2.6 will summarize the above sections.

2.2 Principles for Biosensors

A biosensor is an analytical device for detecting a certain kind of analyte that combines a biological component with a physicochemical detector. Currently, biosensors have been widely utilized and even dominant in many scientific fields. For example, flow cytometry is employed in cell counting, sorting, biomarker detection and protein engineering. This tool has been routinely used in the diagnosis of health disorders [11].

Following are some important criteria for an effective biosensor:

- Cost is always a huge concern in industry and should be kept as low as possible. Ideally, disposable one-time-use devices should be fabricated, which have their advantage in medical practices in term of preventing contamination.
- Sensitivity is usually defined as the lowest concentration of the target analyte that can be detected by such device.
- Accuracy refers to how closely the sensing result is to the widely accepted gold standard.
- Repeatability is required for biosensors, as people would expect comparable data from certain designed devices.
- Selectivity should ideally be as high as possible, as the detected events are expected to be real response from the testing sample.
- Time to result determines how long the technician must wait for the results, once the testing sample is put into the sensing system.

2.3 Point-of-Care Biosensors

2.3.1 Overview of point-of-care biosensors

Fabricated by biological or biomedical micro-electromechanical systems (BioMEMS) technology, which has already been highlighted in medical applications, point-of-care (POC) sensors provide a significant disease diagnosis/treatment method for people living in remote places. The potential of this technology for early disease diagnosis and monitoring has been highlighted in the past decade. Also, such POC

sensors are attracting people's attention, since health-care delivery and clinical management have become more and more personalized. POC sensors are becoming more and more important due to their low cost, high sensitivity, multi-function, and portability.

POC sensors are making a significant impact on the eradication and management of diseases such as HIV/AIDS, malaria, TB, and other diseases caused by infectious agents. Such diseases are the major causes of death and suffering around the world. In 2011, according to WHO, 14-17 million people died of infectious diseases in developing countries. HIV/AIDS, malaria, and TB have been the main causes of global health crises in the 21st century.

Not only for remote areas, POC devices also have a promising future in various biomedical applications, shown in Fig. 2.1. Applications of POC devices range from personalized cases to hospital settings [12].

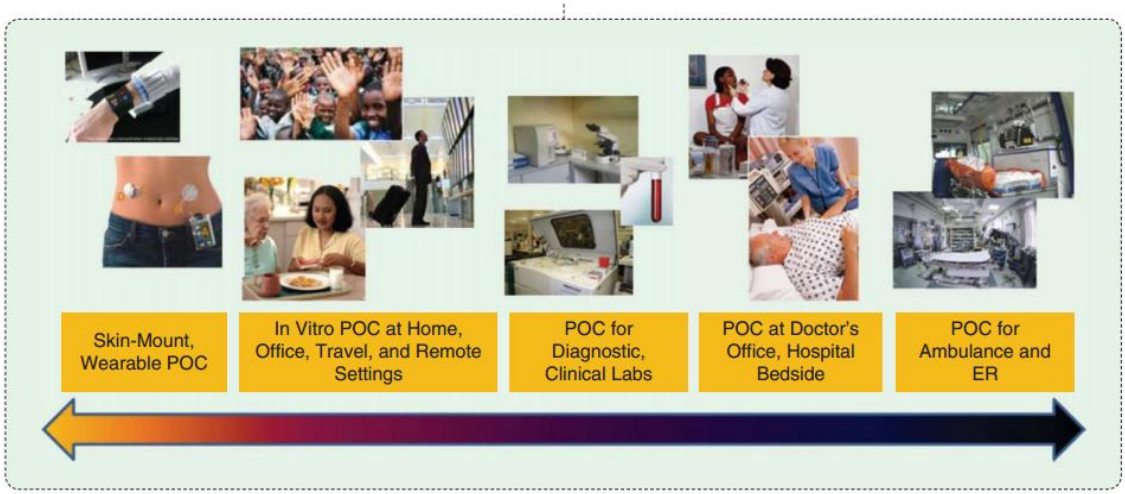

Fig. 2.1 Applications and settings where POC devices can be used [12].

Many current commercial POC diagnostic devices utilize lateral flow tests, which employ a membrane or paper strip to indicate the presence of protein markers such as

pathogen antigens or host antibodies. In the U.S., lateral flow tests are used for diagnosis of a small number of conditions, most notably pregnancy, as well as infections with streptococcus or flu; in developing countries, the lateral flow test is widely used to diagnose HIV [13]. Limitations of such POC devices are less reproducible and less quantitative results, and low sensitivity issues, even though such devices are very easy to handle, inexpensive, and portable.

Another POC device that has been proven to be a reliable and dominant biomedical application is the blood glucose test. Such POC devices have been recognized for their significant impact on diabetic patients' lives [14].

Utilizing BioMEMS technology, POC devices are greatly miniaturized, and many sensing modules could be integrated onto one chip. This greatly expands the functions of POC devices. Such functions, normally performed by large tools or laboratories, are integrated onto miniaturized "lab-on-chip" systems with low cost.

The goals for POC devices are as follows:

- Reducing the sensing process in time, due to the minimized chip size, small sample volume, and higher efficiency
- Improving the sensitivity
- Reducing the amount of reagents utilized each time, to reduce cost
- Making the device a disposable one
- Enhancing the portability of the device

POC devices have a promising future for disease diagnosis and treatment in medical practices, for personalized purposes, and in home medications all around the world, especially in remote places.

2.3.2 Optical sensing method

Optical sensing is a powerful sensing method that has been developed for decades, and has been promoted especially by the invention of the revolutionary strategy, polymerase chain reaction (PCR). After almost 30 years' development, PCR is now a dominant and indispensable technique used in medical practices and biomedical researches [15, 16].

Another successful optical sensing method is flow cytometry, which is now commonly used for cell counting, sorting, and biomarker detection. It can analyze multiple physical and chemical characteristics at the same time, at speeds up to thousands of particles per second. Ever since the first report of modern flow cytometers (basically for cell sorting at that time) in the year of 1965 [17], flow cytometry has been developed at a steady pace. Today, for example, CD4+ T cells are commercially counted by utilizing this tool. Flow cytometers using laser light scattering and laser-induced fluorescence principles are the current gold standard to provide accurate CD4+ T cell counts at high throughputs [18-20].

However, optical sensing methods have their own limitations, such as requiring expensive tools (lasers, etc.), large space, expensive reagents (primers etc.) and so forth. Based on these issues, optical sensing is not an optimal for developing POC devices.

2.4 Planar Electrode Biosensors

Since optical sensing is not the best choice for POC devices, we turn to electrochemical sensors for solutions. The following paragraphs will discuss the work of some of the research groups in studying planar (2D) electrode biosensors.

Among electrochemical methods, large macro-electrodes are commonly used to record cell capture signals [21-24]. Such electrodes, due to their designs, are limited in the sensitivity. Mostly, no single-cell level resolution could be reached by such devices. In this case, smaller electrodes are required, since they are capable of sensing small number of cells. Micro-electrodes can reach such high sensitivity because of their radial diffusion profile as opposed to the planar diffusion profile of macro-electrodes [25, 26]. The capability of detecting a single cell per electrode has been reported in 2012 by Rahman's group, as shown in Fig. 2.2 [27]. It has been demonstrated that the precise counting of CD4+ cells can be achieved by using micro-electrode arrays [28].

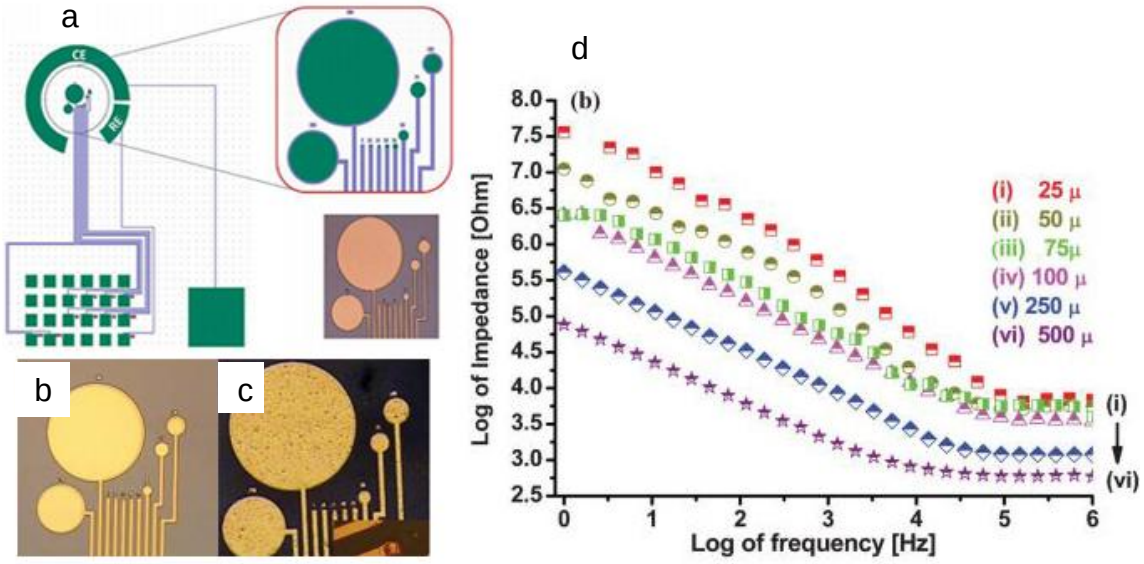

Fig. 2.2 Cell detection utilizing electrochemical impedance technique: (a) Micro-electrode device design; (b) Optical image of blank micro-electrodes; (c) optical image of a cell bounded Electrode; (d) Impedance spectra of 500 to 25 µm designed electrodes in 1 mM FcCOOH [27].

2.5 Hybrid-Nanostructured Biosensors

Nanobiosensors have developed rapidly in the past ten years, among which hybrid-structured nanobiosensors are promising because of their expanded sensing area, rapid testing time, easy fabrication and analysis procedure. Apart from planar electrode devices, researchers have been able to integrate multiple types of structures with totally different morphology onto one device, to improve the capture and sensing ability of certain analytes.

Such 3D nanostructures have been employed for biosensing in many different ways. Such devices have been used for the electrochemical detection of penicillin [5], and proteins [6] including glucose oxidase [7] and West Nile virus [8]. In addition,

hybrid-nanostructured devices are highly recommended for applications to electrochemical impedance spectroscopy (EIS) sensing methods (e.g. DNA hybridization detection) [9] and bacteria sensing [10]. Generally, these detection methods rely on the interaction of the target species at the electrode/electrolyte within the device.

So far, the most commonly used hybrid structure is built by adding a nano-channel membrane on top of the basic substrate. Usually, such a nano-channel membrane is fabricated by making nanopores with regular spacing of high uniformity (e.g. AAO template) [29-30].

Such nano-channel devices have been reported for sensing bacteria [10], virus [31], DNA [32], and other small bioparticles. Nano-channels are highlighted as they can greatly enhance the surface biological interaction area, thus improving the capture efficiency and sensitivity of the device. The nano-channel device and sensing schematic are shown in Fig. 2.3.

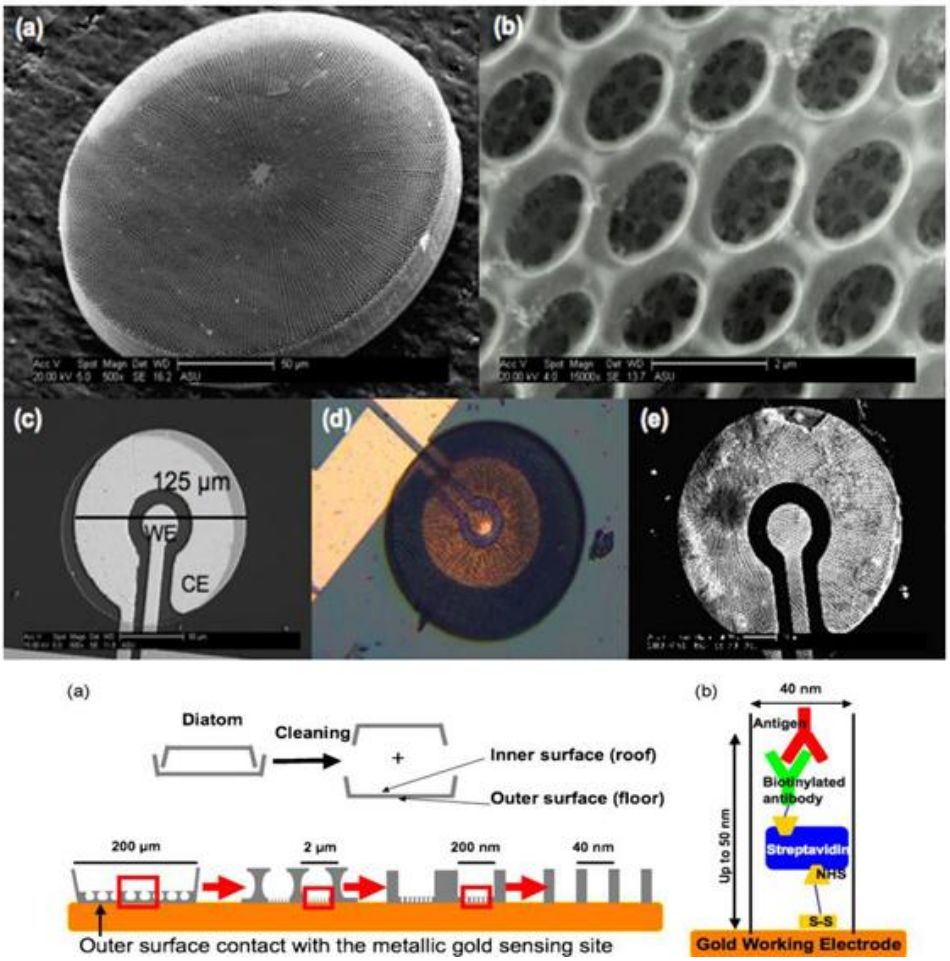

Fig. 2.3 Nano-channel device SEM images, optical images, and sensing mechanism.

Other nanostructures can also improve the device capture and sensing ability. Cancer protein biomarker detection and cancer therapy have been demonstrated by using carbon nanotubes [33]. Implementation of the field-effect transistor based transconductance technique using silicon nanowires has made it possible to detect nucleic acid with high sensitivity [34]. A Si nanoporous template has been demonstrated for protein detection with sensitivity on the order of pg/ml [35].

2.6 Summary

This chapter summarized the current research highlights in making biosensors. It summarized the basic principles of biosensors, as well as the criteria for making them. This background could be helpful in the design of biosensors.

Point-of-care biosensors were illustrated in this chapter. The significance and applications of such devices were discussed, such as the fact that POC devices will be a more obvious choice for medical applications for many reasons. Optical sensing was introduced along with a discussion of why it has served as a dominant tool in many biomedical fields, for example, PCR, ELISA, and flow cytometry. But optical sensing is not compatible for POC devices, as it requires expensive tools, large space, and expensive reagents.

Two major electrochemical impedance sensing methods were introduced—planar electrode biosensors and hybrid-nanostructured biosensors. Planar electrode biosensors are mainly applied to cell detection, as low as single-cell level, while hybrid nanostructured biosensors can be utilized for various sensing applications, such as cell, virus, DNA, protein, etc.

Based on the proceeding discussion, the desired sensing device should be able to meet certain requirements:

- Easy, fast and cheap fabrication
- Short time to result

- Low cost of the entire device
- High sensitivity
- Ability to screen for a wide variety of bioparticles

Based on the requirement of the direct sensing method, a 3D hybrid-nanostructured biosensor is highly desired. Also, an electrochemical impedance spectroscopy (EIS) based sensing method is preferred over optical sensing, in terms of complexity, cost, portability and many other concerns. Thus a nanograss embedded microfluidic device for electrochemical impedance sensing is proposed, according to its low cost, high sensitivity and other merits.

The rest of this thesis will focus on fabricating such a device and getting it to work as expected.

CHAPTER 3. FABRICATION OF NANOGRASS DEVICES

3.1 Introduction

The surface (morphology/surface area/roughness) of the substrate plays a key role in modulating the molecule capture on it. It has been shown in previous studies [36] that posts, made of nanoporous vertically aligned carbon nanotube (VACNT), can trap cancer cells and other tiny objects as they flow through a microfluidic device, as shown in Fig. 3.1.

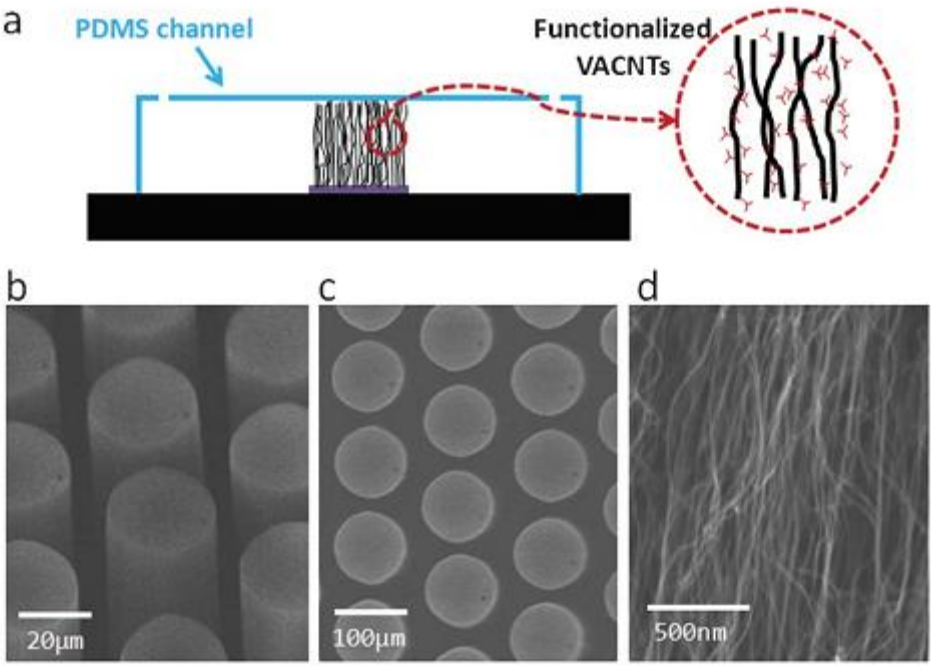

Fig. 3.1 (a) Schematic of a microfluidic device with nanoporous features inside a PDMS channel; (b) SEM angled view of a patterned VACNT post array; (c) SEM top view of a patterned VACNT post array; (d) SEM of the nanostructure of a VACNT forest [36].

For capturing smaller molecules, such as bacteria and virus, no such nanostructure has been designed and fabricated. However, many surface chemistry methods, especially antibody sandwich structures, have been reported for virus capturing [37]. Such antibody/enzyme labeling method not only depends highly on the chemical attachment of the sandwich structures, but also cannot guarantee a highly efficient capture process. Dielectrophoretic (DEP) filter, embedded in microfluidic devices for virus capture, has been determined as an efficient electrical method of virus capturing [38, 39]. Nevertheless, it is not easy enough to operate, especially in remote areas. Therefore, it is greatly beneficial to fabricate nanostructures which are suitable for small molecule (e.g. bacteria, virus) capture and sensing. Section 3.2 will present the fabrication process of Si nanograss, which is the base structure of the nanograss device; Section 3.3 will present the fabrication process of the nanograss capture/sensing device.

3.2 Si Nanograss Fabrication

3.2.1 Nanograss fabrication mechanism

Si nanograss is fabricated by STS Pegasus ICP-DRIE, without using any mask. The key mechanism underlying the nanograss fabrication is the reactive ion nucleation during the reactive ion etching process. In the plasma-enhanced multiple ion reaction system (SF_6, C_4F_8, O_2), the nanoscale gas-to-solid phase transition synchronizes with the nanoscale solid-to-gas phase transition [40], which results in pseudouniform, complex

nanoparticle arrays grown over the surface of the etching substrate. These nanoparticles act as the etch mask for the anisotropic Bosch etching process.

Another factor that affects the etching process is the loading effect, which results from different patterns on the substrate. It is well known that pulsed (time domain multiplexed) deep silicon etching suffers from serious loading effects inherent to reactant transport limited etching [41]. The loading effect is the dependence of the etch rate on the quantity of material being etched [42]. Feature scale pattern dependencies (microloading and aspect ratio dependent etching) and chip/wafer-level loading effects complicate the use of deep silicon etching in MEMS applications [41], because of their detrimental effect on uniformity and etch rate on the wafer scale. Since the device is designed to be bonded with PDMS to make microfluidic chips, micropillars of 40 μm diameter are patterned by the common lithography process, shown as Fig. 3.2 (c). Nanograss is fabricated in the space between the pillars (see Fig. 3.2 (d)), which can be set at 8 μm, 11 μm, 14 μm and 17 μm.

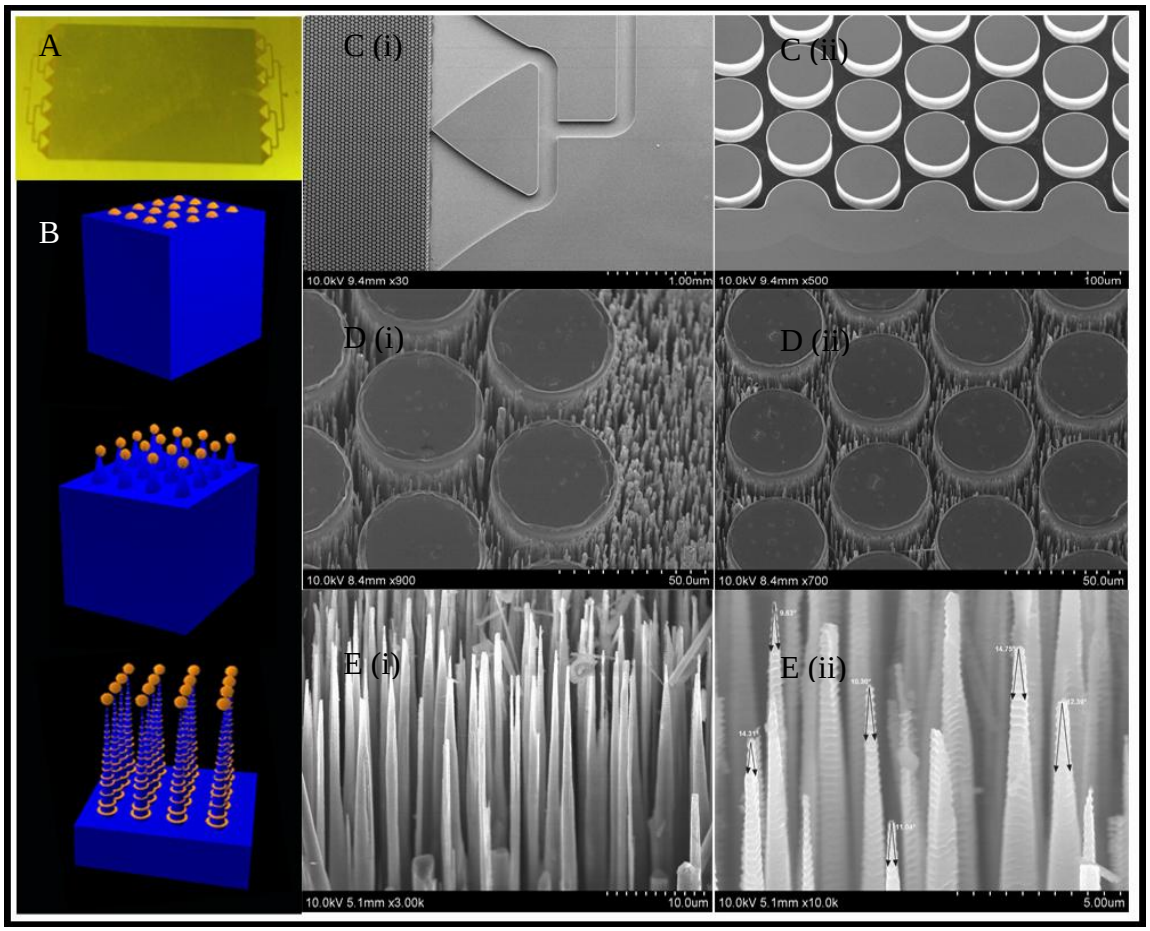

Fig. 3.2 (a) Si nanograss fabricated by STS Pegasus ICP RIE; (b) Process flow of the simultaneous nucleation and etching nanomanufacturing process. Pseudo-uniform silicon oxyfluoride nanoparticles are formed on the silicon substrate surface in the first step. The oxyfluoride nanoparticles grow on top of the Si surface by a gas-to-solid nucleation process, and they act as a protective mask for the subsequent Si etching process; (c) i. Microfluidic channel and micro pillars etched by Bosch process, ii. Magnified image of micro pillars; (d) i. Nanograss is observed in the space between micropillars, and also in the open space; ii. Uniform nanograss fabricated in the space between micropillars; (e) i. Side view of the nanograss, ii. Magnified image of nanograss structures.

3.2.2 Nanograss fabrication process

The nanofabrication process is shown in Fig. 3.2 (b). Bare silicon substrates are cleaned by a standard cleaning process (Acetone, IPA, DI water, and IPA) and treated with a wet etching (Buffered HF-10s) process to remove the native oxide layer on the surface.

In a reactive ion etcher chamber, a silicon nanograss array is formed via Bosch process with a multiple reactive ion mixture of octafluorocyclobutane (C_4F_8-etching), sulfur hexafluoride (SF_6-passivation), and oxygen (O_2). Fluoride ions are the primary etching plasma to react with silicon atoms on the surface layer, while oxygen ions, fluoride ions, and silicon ions together comprise the building blocks to synthesize the complex silicon oxyfluoride compound (SiO_xF_y) on top of the substrate surface layer (see Fig. 3.3) [40]. The simultaneous nucleation and top-down etching reactions can be summarized in two chemical reaction formulas.

$$Si + 4F^- \xrightarrow{Etching} SiF_4$$

$$SiF_4 + O^* \xrightarrow{Synthesis} SiO_xF_y$$

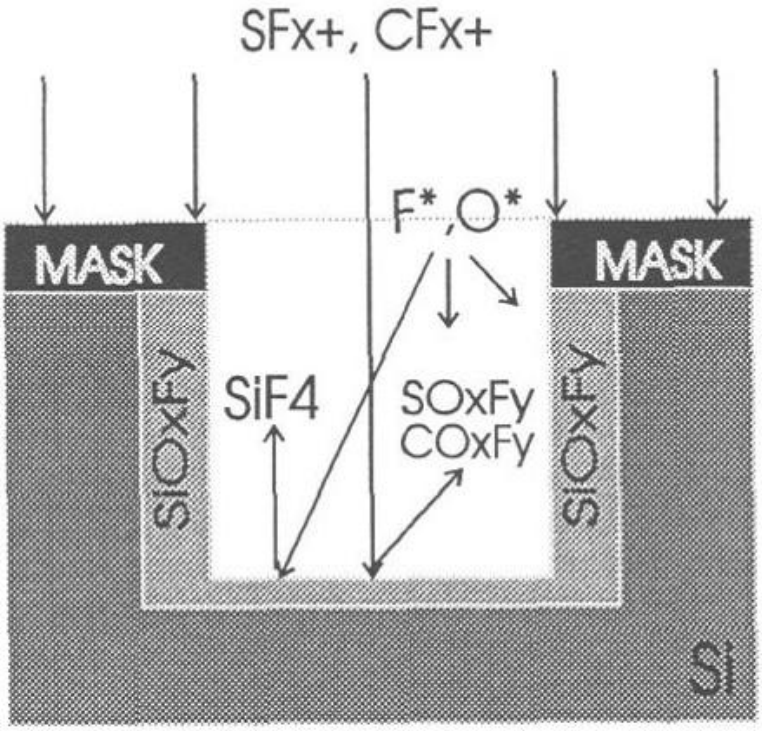

Fig. 3.3 $SF_{x+}/O_2/CF_{x+}$ chemistry and surface SiO_xF_y formation on the sidewall, as a reference for the SiO_xF_y nanoparticle formation on Si surface [40].

Initially, randomly distributed seed spots will be nucleated when fluoride ions and oxygen ions simultaneously meet at some exposed silicon crystal lattice points on the surface [43]. Meanwhile, the seed spots will quickly grow into nanoparticles through a gas-to-solid nucleation process. These nanoparticles are about 1 μm in diameter, shown in Fig. 3.2(d). Thus a protective nanomask array has been formed right before the subsequent etching process. Besides the nucleation process, the exposed silicon surface is anisotropically etched down by C_4F_8. Because C_4F_8 has a very high reaction selectivity of silicon to silicon oxide (200:1), the growing silicon oxyfluoride (SiO_xF_y) nanoparticle

array acts as the etch mask that protects the covered silicon surface. Consequently, the longitudinal nanostructures will be created by the Bosch anisotropic etching process, as shown in Fig. 3.2(e).

A ripple structure can be seen with the sidewall, as shown in Fig. 3.2 (e). The SEM image also shows that the ripple synthesized on the sidewall remains about the same size along the nanograss side wall. The nanoripple structure on the side wall indicates the localized reactive ion nucleation happening at every Bosch cycle [43]. This observation strongly supports the plasma enhanced silicon oxyfluoride nanostructure nucleation mechanism.

Since the Si nanograss density is determined by the density of the SiO_xF_y array, it can be controlled by varying the $C_4F_8/SF_6/O_2$ plasma concentrations. The average height of the nanograss can be controlled by varying the time of the etching process (40 μm after 14 min etching). This nanograss fabrication method can be implemented with a standard reactive ion etcher, without requiring any etching mask (for conventional top-down etching process) or any expensive metal catalyst (for conventional bottom-up synthesis process, e.g. Au).

3.3 Nanograss Devices Fabrication—Metal/Oxide Deposition

To fulfill the capture and sensing function of the nanograss based device, further metal/oxide deposition is needed. Before metal evaporation, the nanograss substrate was treated by O_2 descum (planar plasma etch system) for 1 min to remove the carbon-polymer residue. Using e-beam evaporation, 5 nm titanium (adhesion layer) and then 95 nm gold were deposited onto the nanograss structures to obtain bottom electrode structure needed for electrical connection. Good electrical contact has been achieved based on the metal deposition. The process flow is shown in Fig. 3.4 (a); nanograss structure with deposited Au is shown in Fig. 3.4 (b).

Above the Au electrode structure, another layer is required to protect the captured biomolecules from directly contacting the Au electrode [44]. We deposited a 100 nm Al_2O_3 layer on top of Au electrode structure by using an ALD system (Cambridge NanoTech Atomic Layer Deposition System). A 200-cycle Al_2O_3 on Si sample is shown in Fig. 3.4 (c) to indicate the surface morphology/roughness of the Al_2O_3 layer. ALD Al_2O_3 is employed here according to its highly conformal property after deposition, even on high aspect ratio structures such as nanograss. With the deposited Al_2O_3 layer, not only will the chemical interaction at the nanograss surface will be greatly enhanced, but also the Al_2O_3 layer turns the interaction surface highly hydrophilic, which helps greatly improve the capture efficiency [44].

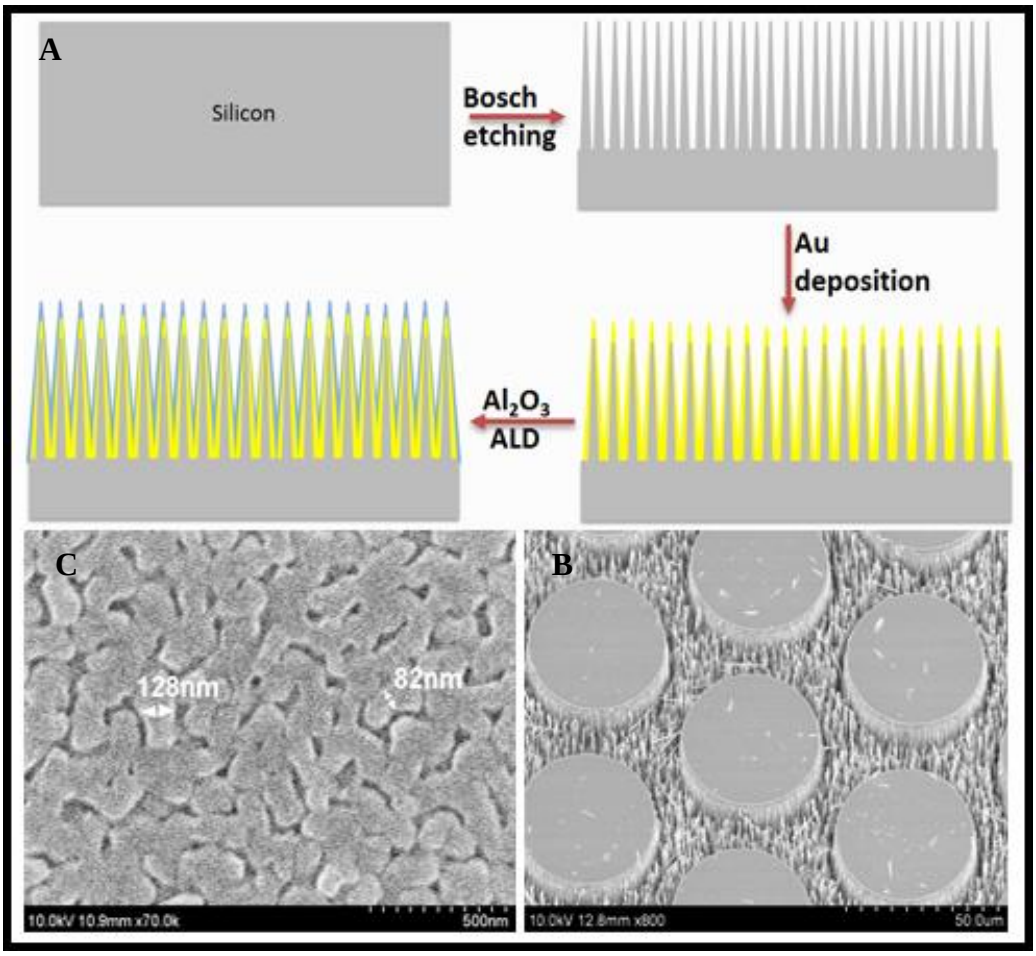

Fig. 3.4 (a) Schematic of the process flow of metal/oxide deposition; (b) SEM image of nanograss structure after Au deposition; (c) SEM image of an ALD Al_2O_3 sample—200 cycles on Si substrate.

CHAPTER 4. CHARACTERIZATION OF NANOGRASS SUBSTRATE

4.1 Introduction

This chapter will present the results of different characterizations of nanograss substrates to investigate substrate properties. The mechanical capture capability is investigated by flowing a solution of fluorescent beads into the nanograss devices, and observing the capture effect under fluorescent microscope. A control experiment is performed by using a similarly designed device but without nanograss embedded.

Super-hydrophobicity is also observed by measuring the contact angle of water droplets (same volume) on the device surface. Hydrophobicity is compared for bare Si surface, micropillar surface, and micropillar with nanograss surface. Surface enhancement Raman spectroscopic (SERS) effect is also tested on the device substrate. Section 4.2 will present the capture efficiency experiment based on fluorescent beads. Section 4.3 will present the surface hydrophobicity test. Section 4.4 will present the SERS test on different concentrations of a common dye – Rhodamine 6G.

4.2 Capture Capability of Nanograss Device

This section will discuss the preparation of the nanograss devices, fluorescent bead solution and the image analysis for the study of flowing fluorescent beads into two devices— with and without nanograss embedded.

4.2.1 Device preparation

To test the capture efficiency of nanograss devices, microfluidic devices were fabricated based on the strategy shown in Chapter 3. Devices with and without nanograss were fabricated by different etching process conditions (see Chapter 3 for details). Pillars were fabricated to serve as supporting structures, which were bonded to PDMS on top. Nanograss was fabricated in the spacing between micropillars, without any mask, by Bosch etching process. Images of the devices are shown in Fig. 4.1.

Figure 4.1 (a, b, c) show optical images of the device flow test with fluorescent beads solution of uniform concentration. Figure 4.1 (a) shows the experiment setup: PDMS was bonded on top of the microfluidic device, and then fluorescent bead solution was flowed into the device through tubing. Figure 4.1 (b) shows the basic chamber device, without any micropillars and nanograss; Fig. 4.1 (c) shows the image of a microfluidic device with micropillars and nanograss.

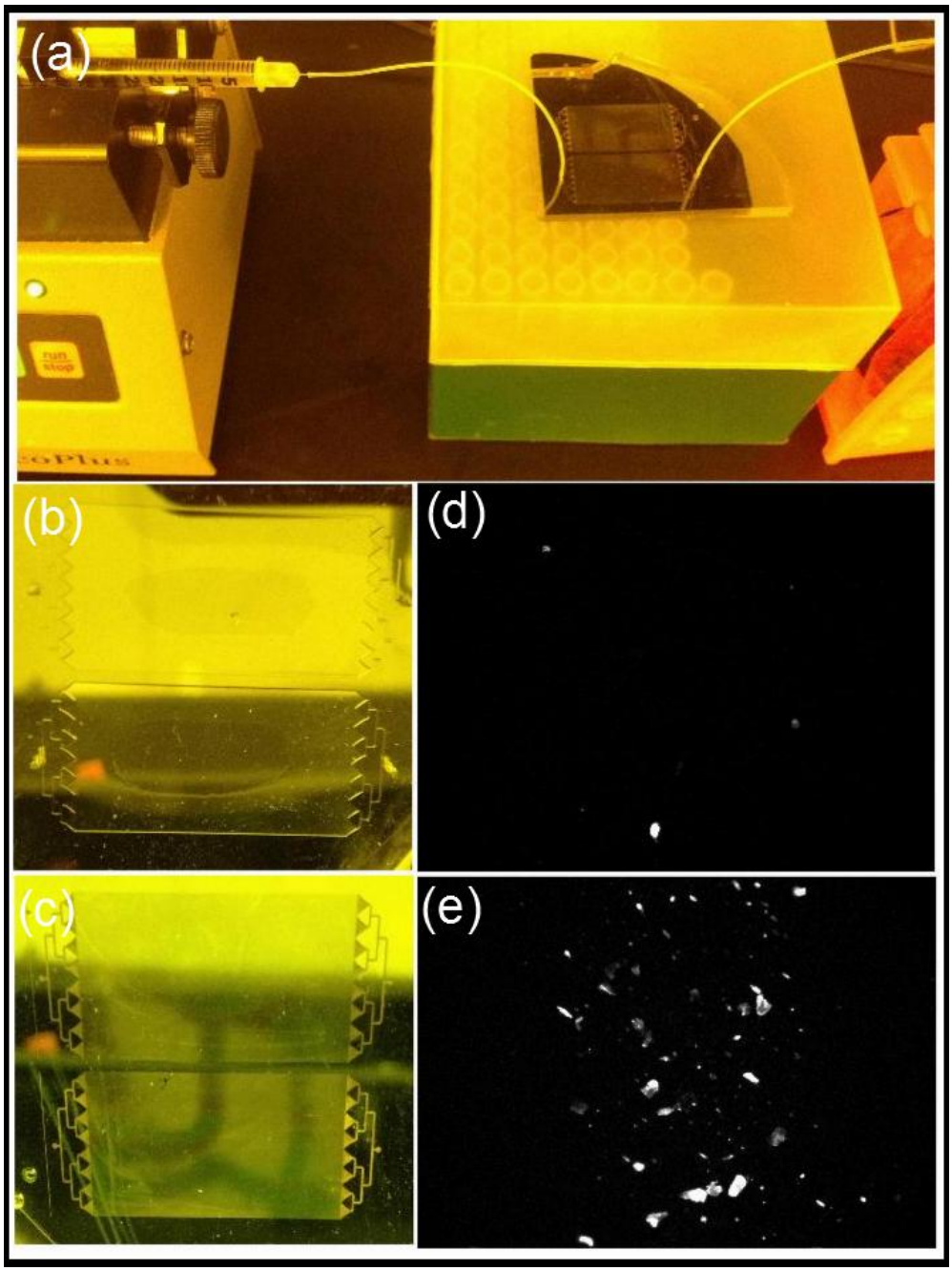

Fig. 4.1 Flow test with Nile Red fluorescent beads: (a) Capture experiment being performed on nanograss device; (b) Optical image of basic chamber device; (c) Optical image of nanograss device; (d) Fluorescent image of basic chamber device after flowing through fluorescence beads; (e) Fluorescent image of nanograss device after flowing through fluorescence beads.

4.2.2 Capture efficiency test

To test the particle capture of the nanograss device, Nile Red fluorescent beads (0.53 μm in diameter) were employed. Fluorescent beads were diluted in 1x PBS at 1:1000 and then flowed into both the nanograss device and basic chamber device (control) at 10 μL/min for 10 min, to ensure thorough flow through the devices. We used the standard infusion syringe pump from Harvard Apparatus (Harvard Apparatus, Holliston, MA).

Figure 4.1 (d, e) show fluorescent images of the devices with and without nanograss, respectively; both devices were detected under fluorescent microscope with TRITC fluorescent filter.

By comparing Fig. 4.1 (d) and (e), we can clearly tell the difference in physical capturing ability between nanograss and basic chamber devices.

4.2.3 Image analysis

In order to observe mechanical capture ability of nanograss devices, fluorescence images were acquired. The experiment consisted of the following two observations:

(a) fluorescence derived from the beads that were captured by basic chamber device (control experiment), and

(b) fluorescence derived from the beads captured by nanograss embedded microfluidic devices.

Fluorescent images of the beads captured on chip were analyzed using ImageJ software. The criteria for the analysis were the numbers of total fluorescent beads captured, and the number of particles for different fluorescent intensities. The total number of fluorescent beads was obtained from the counts of particles for different fluorescent intensities, shown in Fig. 4.2.

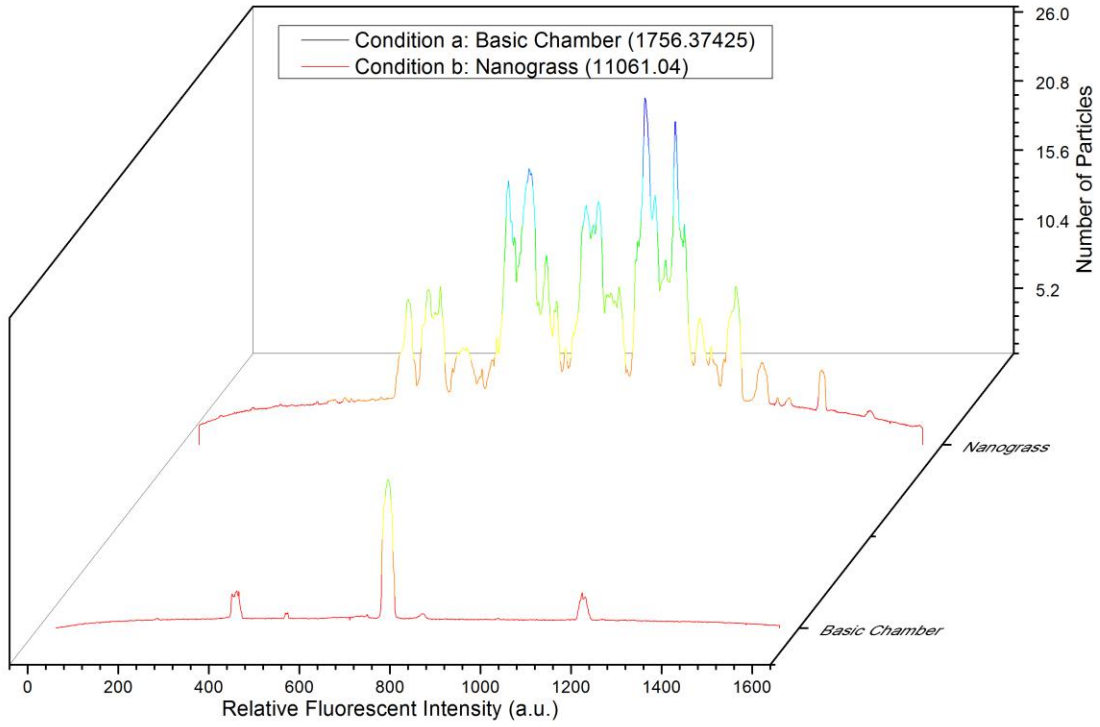

Fig. 4.2 Image analysis of fluorescent beads captured by basic chamber and nanograss microfluidic devices. X-axis is the relative fluorescent intensity; Y-axis is the number of particles of each fluorescent intensity; Z-axis represents two devices we tested—basic chamber and nanograss microfluidic devices.

Fluorescence distribution of the beads for the aforementioned two conditions is shown in Fig 4.1 (d, e). The images were acquired right after the capture experiment, following the protocol given in Fig 4.1 (a). From Fig. 4.2 we observed clearly that the increase of fluorescence intensity indicated more beads captured by the devices. The values were calculated from acquired images of fluorescent beads. The relative fluorescence intensity (X-axis) could also be expressed as gray level, as adopted by many researchers [45], to indicate the number of beads captured at a certain spot. Condition b (nanograss device) shows much greater fluorescent intensity and more particles than condition a (basic chamber device). By simply doing integration for conditions a and b, we can get the total number of fluorescent beads that were captured under each condition. Beads captured by the nanograss device were about one order of magnitude more numerous than those captured by basic chamber device (11061 vs. 1756). This indicates the different mechanical capture abilities of the two devices.

4.3 Super-Hydrophobicity Test

The results about the hydrophobicity of the substrates with different surface morphology will be presented and discussed in detail in this section.

4.3.1 Surface morphology and surface hydrophobicity

Super-hydrophobicity is also observed on the device surface by measuring the contact angle with a goniometer. With the microstructure of micropillars, surface hydrophobicity is greatly enhanced, as shown by comparing Fig. 4.3 (a) and (b).

Embedding with nanograss, which is shown in Fig. 4.3 (c), the device surface is highly hydrophobic, with the contact angle of 155 °(water). On the other hand, when flipping the device more than 90 °, shown in Fig. 4.3 (d), the droplet still stays on the substrate.

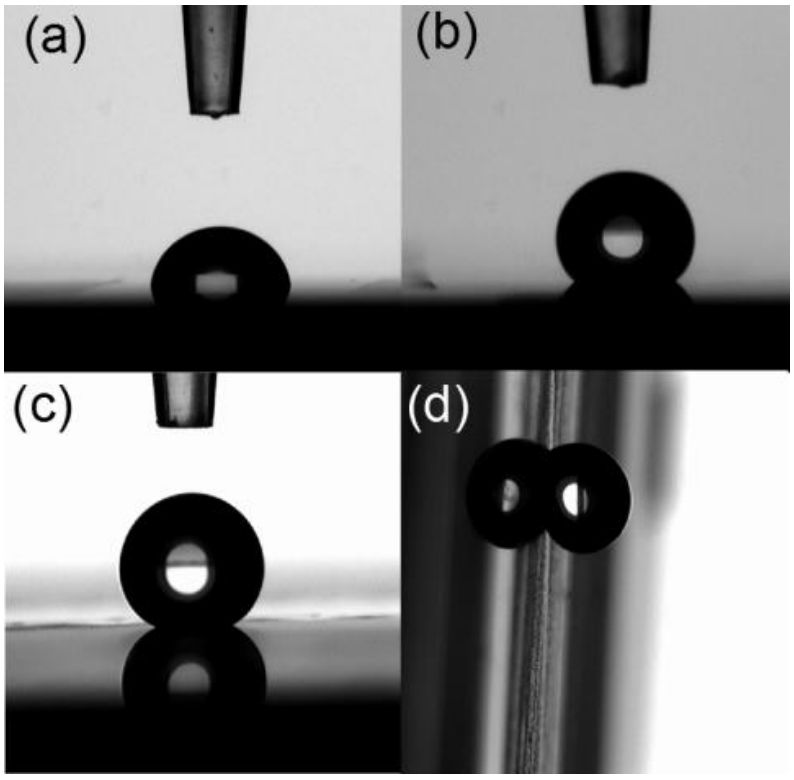

Fig. 4.3 Contact angle measurements for different substrates: (a) 83.519 °for plain Si surface; (b) 139.059 °for Si pillar surface; (c) 154.781 °for Si pillar with nanograss surface; (d) Petal effect is observed when flipping the device more than 90 °.

Surface morphology of the Si micropillars substrate and nanograss embedded substrate is illustrated by the SEM images in Fig. 3.2 (c-ii, d-ii). Figure 3.2 (c-ii) shows a periodic array of micropillars with uniform diameter of 40 μm and height of about 40 μm, with spacing of 11 μm in between. Figure 3.2 (d-ii) shows the nanograss fabricated by Bosch-like etching process, with diameter of 1-2 μm and height of about 40 μm.

The hydrophobicity of a certain surface can be greatly enhanced by embedding different micro- and nanoscale structures. In nature, the surface of the lotus leaf is noted for its self-cleaning property, which is induced by the roughness at two length scales amplifying the intrinsic hydrophobicity—known as the lotus effect. Similarly to this, our device's surface also exhibits super-hydrophobicity with a contact angle of about 154.781°, shown in Fig. 4.3 (c), owing to the micropillars along with the nanograss embedded in between. Also in nature, water droplets of certain volume can stay pinned to the surface of a red rose petal. Similarly, water droplets on the "petal" (our device) surface maintain their spherical shape whether the surface is horizontal or vertical (Fig. 4.3 (d)), showing a high contact angle hysteresis. The crucial parameter for this effect is the volume of the droplet. For a small droplet, the weight is small compared to the surface tension force, and thus it is expected that a droplet will stick to the surface. When the volume of the water droplet is ~10 μL, a balance of the weight and the surface tension is reached, above which the droplet will fall.

4.3.2 Theoretical analysis

In general, surfaces with a static contact angle higher than 150° are defined as super-hydrophobic surfaces. There are two causes for super-hydrophobicity: (1) the liquid attaches to the solid surface (Wenzel's state), and (2) it leaves air inside the texture (Cassie's state) [46]. The Wenzel model describes homogeneous wetting by the following equation [47]:

$$\cos\theta_w = r\cos\theta_y$$

where θ_w and θ_y are the Wenzel contact angle and the Young contact angle, respectively, and r is the roughness ratio, defined as the ratio of the true surface area to its projected area.

The Cassie model describes heterogeneous wetting by the following equation:

$$\cos\theta_w = r\cos\theta_y$$

where θ_c and θ_y are the Cassie contact angle and the Young contact angle, respectively, r is the ratio of the actual area to the projected area of the solid surface that is wetted by the liquid, and f is the area fraction of the projected wet area.

As for the details of contact angle hysteresis, Wenzel's state can induce a high contact angle hysteresis and Cassie's state a low contact angle hysteresis. An important super-hydrophobic Cassie impregnating wetting state needs to be addressed here [48, 49].

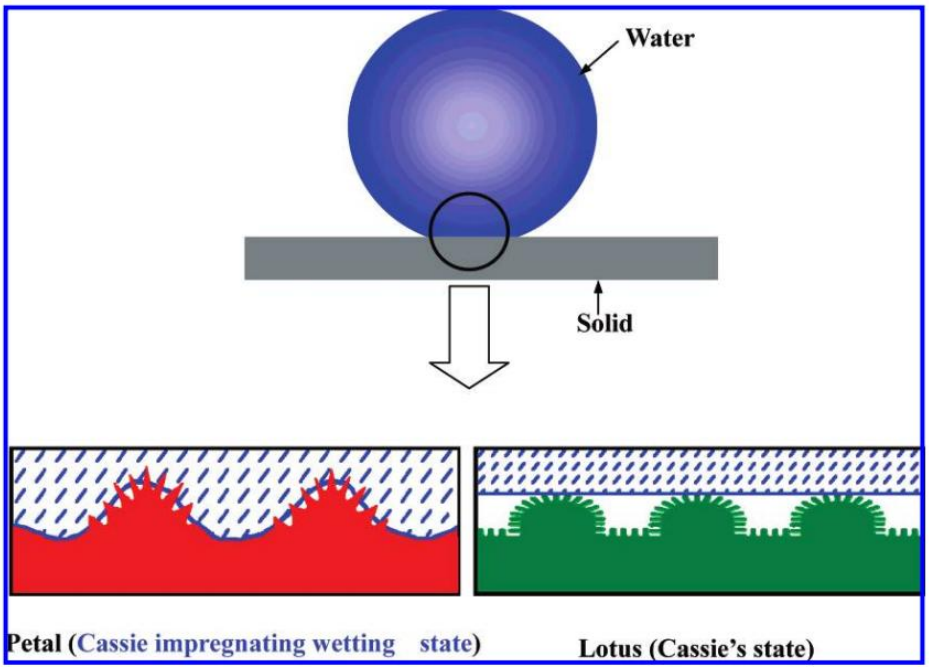

Fig. 4.4 Schematic illustrations of a drop of water in contact with the petal of a red rose (the Cassie impregnating wetting state) and a lotus leaf (the Cassie's state) [49].

As shown in Fig. 4.4, for the Cassie impregnating wetting state, grooves of the solid are wetted with liquid and solid plateaus are dry. This state is described by different equations from those for the Wenzel and ordinary Cassie wetting states. In this regime, the liquid film impregnates the texture; however, there will always remain islands that emerge above the "absorbed" liquid film. On the basis of the hierarchical micro- and nanostructures on the surface of the petal and the duplicated polymer, it could be suggested that rose petals, when both contact angles and adhesion are large, are in the Cassie impregnating wetting state [49].

As to the petal effect, hierarchical micro- and nanostructures are fabricated. Water droplets are expected to enter into the larger scale grooves of the micropillars but not into the smaller nanograss, thus forming the Cassie impregnating wetting regime [50-52]. It

can be readily understood that water sealed in Si micropillars would cling to the nanograss surface, showing a high contact angle hysteresis in the range of volume when the surface is tilted vertically.

4.4 SERS Effect for Nanograss Devices

Microfluidic devices have been widely used for Point-of-care (POC) diagnostics due to portability, shortened processing time, and easy operation [53]. The application of surface-enhanced Raman scattering (SERS) to measure different biochemical species is highly valued for its ultra-sensitivity and multiplex targeting [54]. We demonstrate SERS on our nanograss-embedded microfluidic devices with a common fluorescence dye, Rhodamine 6g (R6G). As a preliminary study, we flowed R6G [55], an even smaller molecule (diameter ~1.24 nm) than a virus (most range in size from 5 to 300 nm), through our device and detected, by SERS, spectra at different concentration levels. Ti and Au were deposited on top of the nanograss structures by e-beam evaporation. Gold-coated ripples serve as plasmonic structures after metal deposition. With R6G used as a Raman probe, we found that Raman signals were greatly amplified. Figure 4.5 shows the representative SERS spectra of R6G at different concentrations. The relative intensities of SERS signals decreased with serially diluted solutions. We can clearly identify the primary Raman peak signature down to the concentration of 1 μM.

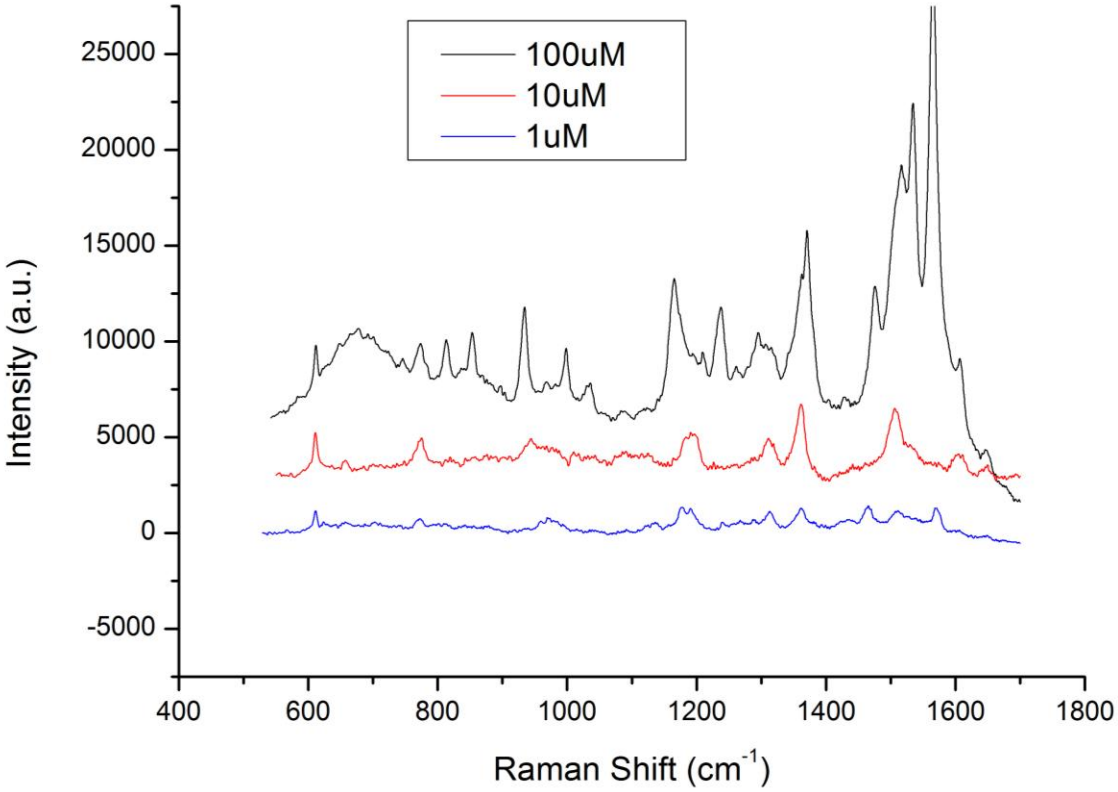

Fig. 4.5 Representative SERS spectra of serially diluted R6G solutions spotting on the substrate surface, from 100 μM down to 1 μM.

CHAPTER 5. FINITE ELEMENT SIMULATION FOR NANOGRASS EMBEDDED MICROFLUIDIC DEVICES

5.1 Introduction

Before running the microfluidic flow test on nanograss embedded microfluidic devices, certain flow parameters are required to get a brief understanding beforehand. In this case, a 3D physiologically relevant model for fluidics flowing through the microfluidic chamber is urgently needed in this research. Due to measurement limitations, it is difficult to control the flow testing characteristics and the entire process is time-consuming and expensive. To overcome these limitations, we developed a simple microfluidic system using polydimethylsiloxane (PDMS) to serve as the reaction environment under physiological flow. The flow characteristics such as streamline directions, shear stress profile, and velocity profile inside the microfluidic system were first examined computationally using a COMSOL Multiphysics simulation (COMSOL Inc., Burlington, MA).

5.2 COMSOL Multiphysics Simulation

Assuming a 3D chamber structure, we carry out the simulation within a periodic cell of an array of 2 μm by 40 μm nanograss. Different velocity is imposed into the chamber in order to investigate the fluidic characteristics in the chamber. The fluid

volumetric flow rate is varied from 10 μL/min to 100 μL/min. Water is used as the fluid for the simulation to get an understanding of the flow test.

Table 5.1 Simulation Parameters

Parameter	**Value**
PDMS chamber height	40 μm
Nanograss radius	1 μm
Nanograss spacing	2 μm
Device width	190 μm
Flow rate	10-100 μL/min
Viscosity	1.3e-3 Pa*s

Parameters for running COMSOL multiphysics simulation are listed in Table 5.1. By using COMSOL Multiphysics simulation, we are able to learn how the flow velocity, pressure, and shear stress vary with flow rate. An empty chamber was set as a control. We found out that maximum velocity, maximum pressure, and maximum shear stress vary linearly with the flow rate. In addition, the parameters above were much greater in the nanograss device than in the control. Figure 5.1 shows the simulation schematics and data analysis.

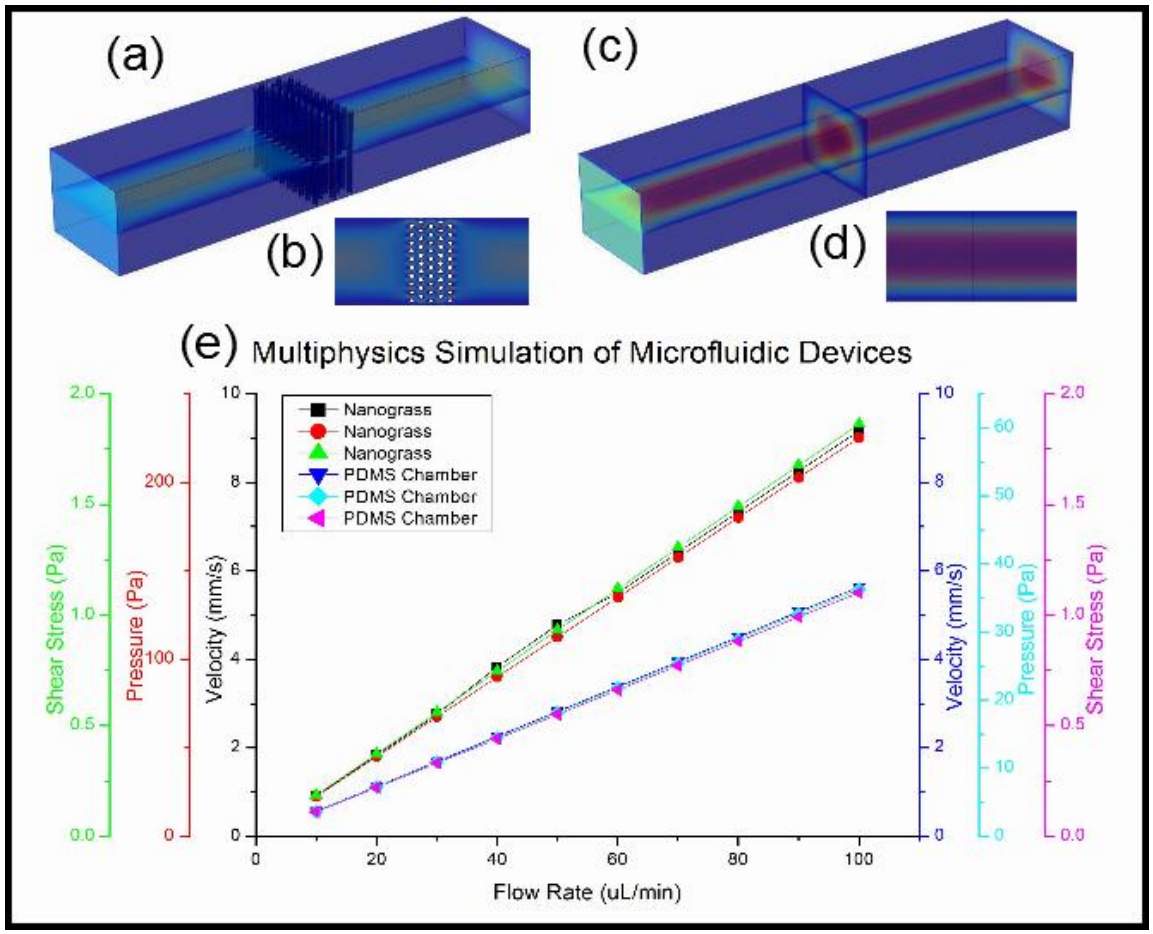

Fig. 5.1 COMSOL Multiphysics simulation schematics and data analysis, diameter of the nanograss was set at 2 μm, spacing was set at 2 μm. Flow rate was varied from 10 μL/min to 100 μL/min at the interval of 10 μL/min: (a) Simulation schematic of nanograss device at the flow rate of 10 μL/min; (b) 2D top view of the simulation on nanograss device; (c) Simulation schematic of basic chamber device at the flow rate of 10 μL/min; (d) 2D top view of the simulation on basic chamber device; (e) Data analysis of maximum velocity/pressure/shear stress against flow rate.

CHAPTER 6. BIOPARTICLE CAPTURE AND IMPEDANCE SENSING OF NANOGRASS-BASED MICROFLUIDIC DEVICES

6.1 Introduction

This chapter presents the results of capture and sensing on nanograss embedded microfluidic devices. We used microfluorescent beads of 500 nm diameter (Spherotech, Inc., Lake Forest, IL). Such fluorescent beads can be used for mimicking small bioparticles flowing through the microfluidic device. Section 6.2 lists the methods of carrying out the experiment. Section 6.3 lists the results and discusses them, and Section 6.4 concludes the chapter.

6.2 Materials and Methods

This section will discuss the preparation of the device, fluorescent beads and experiment setup during the study of capture and sensing experiment.

6.2.1 Device preparation and fluorescent beads

The devices used in this experiment were prepared in exactly the same way as listed in Section 4.2.

The fluorescent beads were obtained from the supplies, and then diluted in serial dilutions. First of all, the fluorescent beads were diluted by 1:1000 into 1x PBS solution. Then a serial dilution was made: 1:10k, 1:100k, 1:1000k, 1:10M, 1:100M.

The fluorescent bead solution was injected through the microfluidic device by Standard Infusion Syringe Pump (Harvard Apparatus, Holliston, Massachusetts). Tubings were put at the edge port of the microfluidic chamber. Two electrodes were placed at the bottom layer of the device and through the PDMS on top of the solution. Both electrodes are fixed steadily to minimize the measurement errors. The experiment setup is shown in Fig. 6.1.

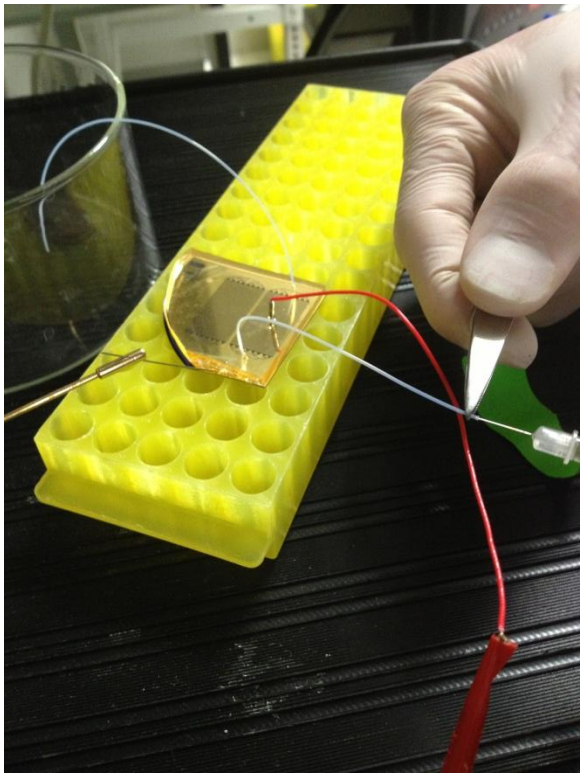

Fig. 6.1 Optical image of the experiment setup.

Once the fluorescent beads were flown into the device, they got captured by the nanograss embedded in the microfluidic device. These captured beads would lead to impedance change that could be measured by the LCR meter (Inductance (L), Capacitance (C), and Resistance (R)). The schematic of the experiment is shown in Fig. 6.2.

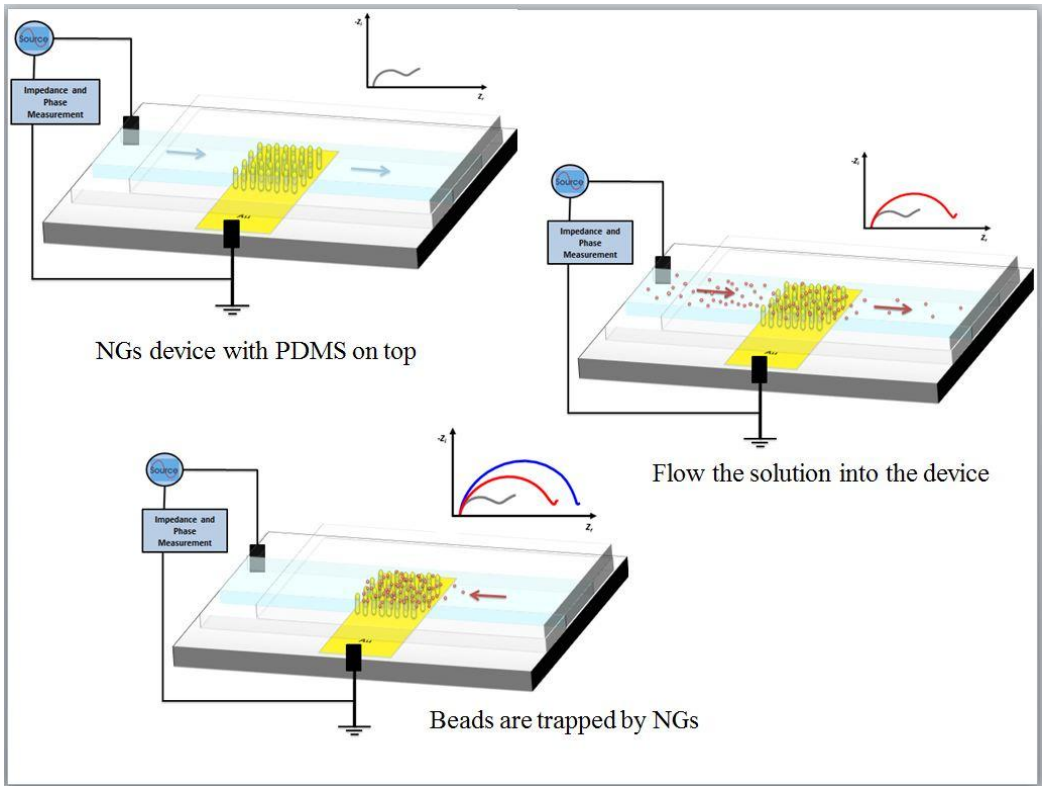

Fig. 6.2 Schematic of the experiment.

6.3 Results and Discussion

The results of the impedance sensing based on the nanograss embedded microfluidic device will be presented and discussed in detail in this section.

6.3.1 Impedance sensing of fluorescent beads in PBS

The evaluation of impedance on nanograss is a frequency-dependent measurement, by which fluorescent beads are attached on the surface of the electrode, nanograss in this case, according to the free flow of charge carriers (i.e. electrical current) from the electrode into the bulk electrolyte. For a wide frequency range, the electrical current passing through a bead–electrode–electrolyte system is paracellular, where it has to bypass the bead along shunt pathways, i.e., through narrow channels that exist between the bead and electrode surface and along the pathways that may exist around the bead into the bulk electrolyte. In order to monitor the bioelectrical impedance response of beads to an analyte, it is necessary to examine the impedance signal at an optimal frequency where the greatest contribution to the measured impedance is due to the injected beads.

The optimal frequency of our cell impedance sensor platform was determined by performing an impedance spectral sweep within the kHz frequency range to compare the impedance signal to that of the bead-free (baseline) one. This range was chosen to make sure of monitoring impedance before beads become incorporated into the overall system impedance at higher frequencies (e.g., in MHz range). Figure 6.3 shows the impedance magnitudes of the frequency-dependent spectrum before and after fluorescent beads were injected into the device.

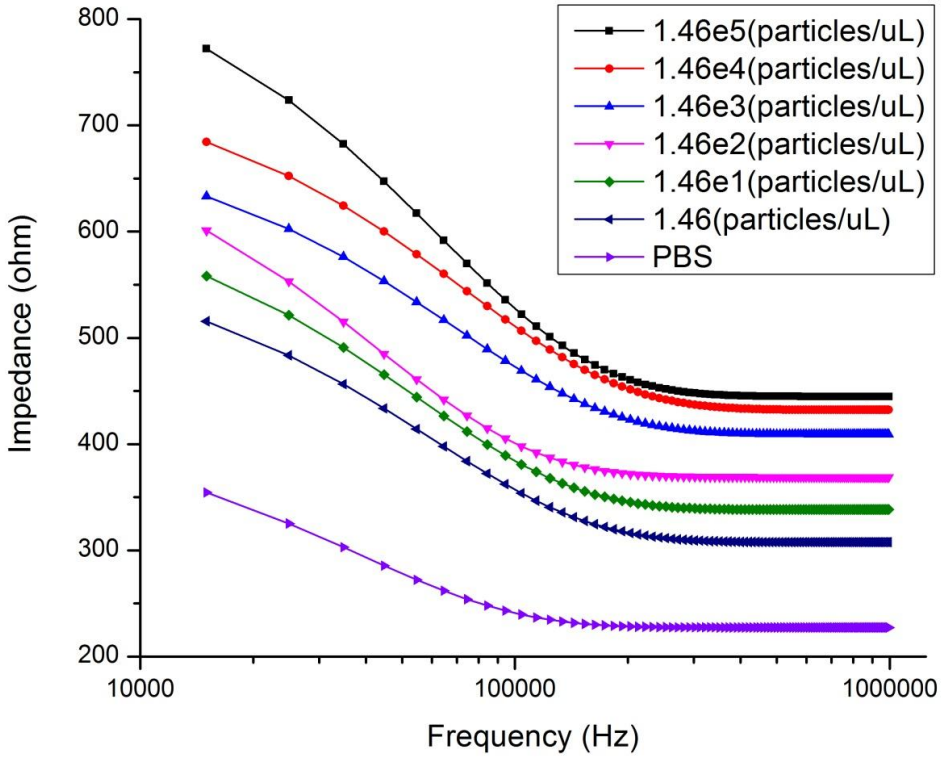

Fig. 6.3 Frequency spectroscopy plot of impedance magnitude |Z| for a frequency range from 10 kHz to 1000 kHz when fluorescent beads are captured by nanograss embedded microfluidic devices.

It is clearly observed that impedance varies with the concentration of fluorescent beads. In the nanograss impedance measurement system, the lower end of the spectrum (low frequency) showed that the detectable impedance was dominated by the electrode–electrolyte interface rather than the presence of beads and bulk solution, which yielded quite clear differentiation for each concentration, respectively. At the higher end of the frequency spectrum (high frequency), the detectable impedance was dominated by the electrolyte and system wiring ultimately acting as a short circuit for frequencies greater than 50 kHz, where bulk solution would dominate the impedance magnitude [56].

In this study, 100 kHz was selected as the designated frequency for impedance measurements reported versus different bead concentrations. At this frequency, an increasing trend was observed for the impedance with the concentration of the beads. To examine the ability of the impedance spectra to discriminate bead concentrations, we plotted impedance magnitude at 100 kHz versus bead concentration for the nanograss embedded microfluidic device.

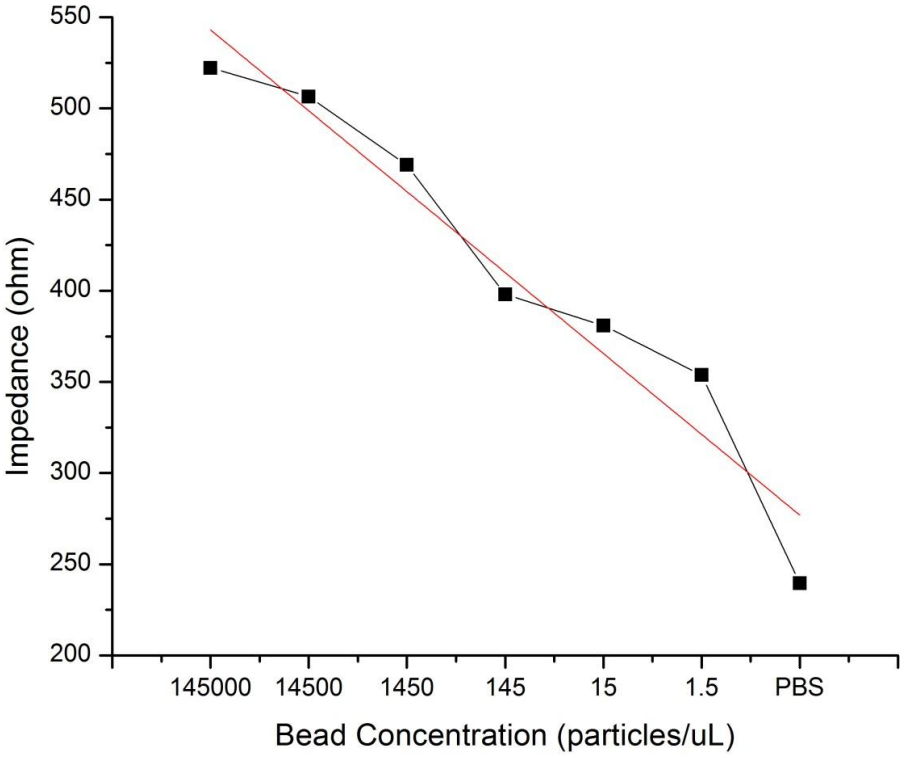

Fig. 6.4 Impedance spectra vs. different concentrations of fluorescent beads at 100 kHz.

The response of impedance magnitude to bead concentration is linear in a log scale plot. This indicates that the impedance caused by beads and the subsequent

conductance of the medium in which the beads are diluted is proportional to the number of beads (see Fig. 6.4). Moreover, using nanograss embedded microfluidic device to detect bioparticles appears to be extremely sensitive, and can detect as few as several beads per microlitre.

6.3.2 Impedance sensing of control experiments

Since the fluorescent beads come in DI water (1:99), we did a control experiment to rule out the effect of DI on impedance change. DI water is diluted in PBS at 1:1000, and a serial dilution is conducted to make the concentration of DI water as low as 1e-7.

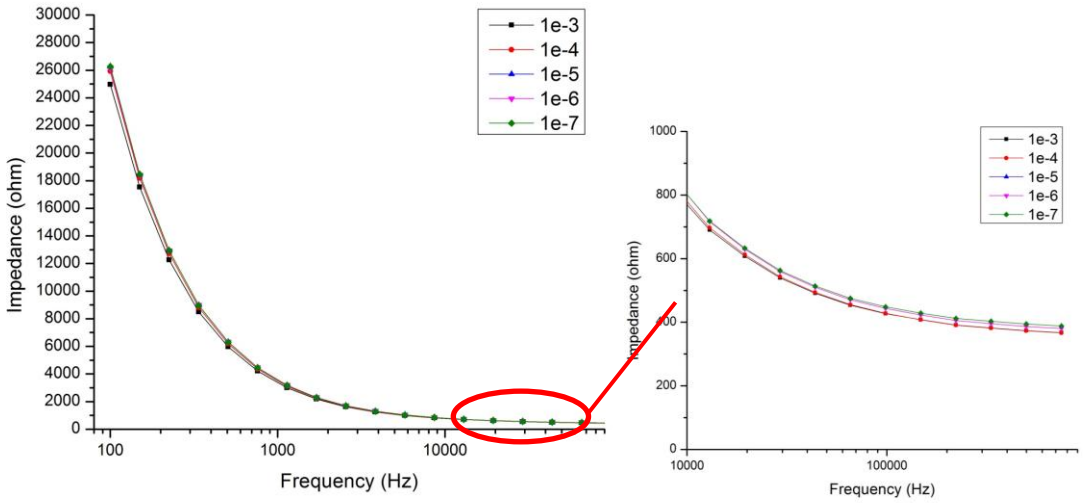

Fig. 6.5 Frequency spectroscopy plot of impedance magnitude |Z| for a frequency range from 100 to 100 kHz for different concentrations of DI water in PBS.

As we can see from Fig. 6.5, there is barely any impedance change for different concentrations of DI water in PBS. Based on this, we can conclude that the impedance change for different concentrations of fluorescent beads is actually due to the beads.

Another control experiment is conducted to test the sensing ability of the nanograss embedded microfluidic device for bulk electrolyte solution. 1x PBS is diluted in DI water by a serial dilution, as low as 1e-5 in concentration. Figure 6.6 shows the impedance spectroscopy plot.

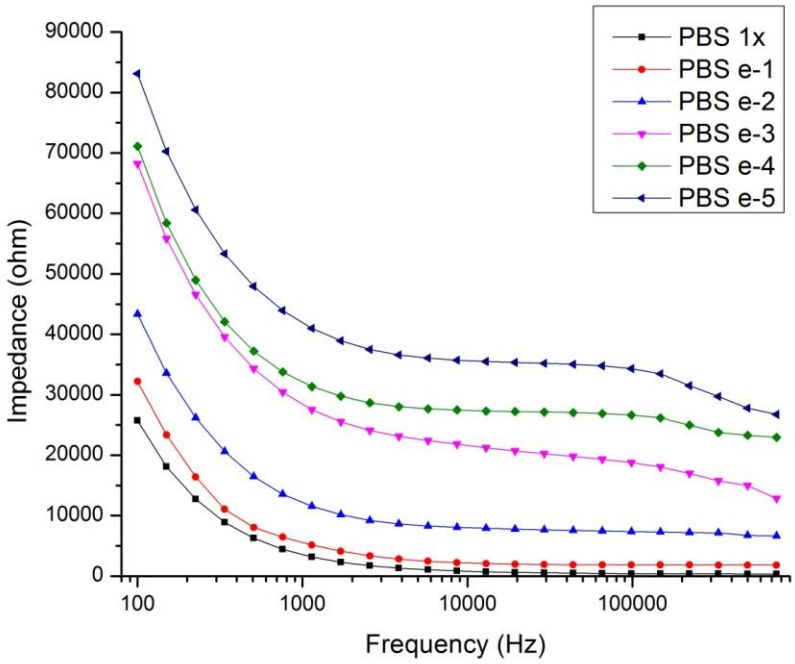

Fig. 6.6 Frequency spectroscopy plot of impedance magnitude |Z| for a frequency range from 100 to 1000 kHz for different concentrations of PBS in DI water.

At high frequency (>10 kHz), impedance is relatively steady and differentiated for different concentrations of PBS in DI water, which indicates the high sensitivity of bulk electrolyte solution for nanograss embedded microfluidic device.

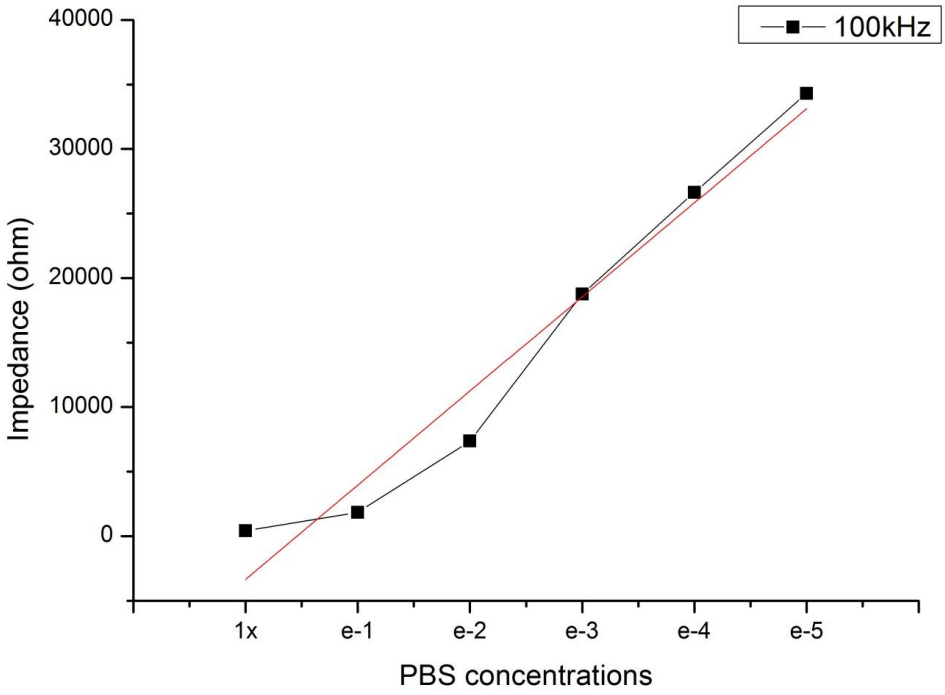

Fig. 6.7 Impedance spectra versus different concentrations of fluorescent beads at 100 kHz.

The response of impedance magnitude to PBS concentration is linear in a log scale plot (see Fig. 6.7), similar to the relationship between the resistance of a simple electrolyte solution and solute concentration [57].

6.4 Principles of Electrochemical Impedance Spectroscopy

Electrochemical impedance model was obtained with a general equivalent circuit in the presence of a redoxprobe (Randles model shown in Fig. 6.8), a model that has been well explained [56-59].

The circuit includes the ohmic resistance of electrolyte solution, R_2, the Warburg impedance, W, which resulted from the diffusion of ions to the electrode interface from the bulk of the electrolyte, the double layer capacitance, C, and the electron transfer resistance, R_1.

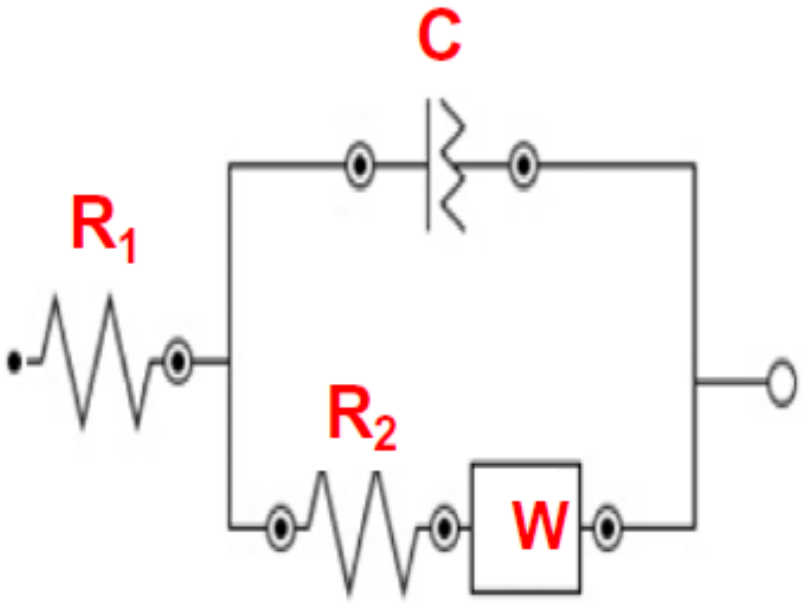

Fig. 6.8 Impedance model circuit.

In detail, R_1 is mainly monitored for conductivity studies. W is generally used for measuring effective diffusion coefficients. Charge-transfer resistance R_2 (also indicated as R_{ct} in many references) and double-layer capacitance C are the parameters used most for analytical detection and sensor/biosensor applications. The measurements are generally performed in Faradaic mode, monitoring the variations of the charge transfer

resistance (R_{ct}) between the solution and the electrode surface. By monitoring the value of R_{ct} after each modification step of the biosensing protocol, the biorecognition event can be carried out with remarkable sensitivity [60].

6.5 Conclusion

This study showed that the nanograss microfluidic device has great sensitivity for both surface-attached particles and bulk electrolyte solution. It has been determined in Section 6.3.1 that the impedance increases when the concentration of the fluorescent beads increases; on the other hand, the impedance decreases when the concentration of the bulk electrolyte increases.

In this study, it has been shown that a nanograss-embedded microfluidic device can be used to capture and sense simultaneously on a single device. The nanograss structure can reach up into the solution for efficient particle capture. Conventional sensors are not able to capture molecules before sensing; here we integrate capture and sensing into one step. This can be used for on-site bioparticle monitoring.

This impedimetric method is much faster (~10 min) than ELISA (~12 hours), which also requires an expensive and complicated antibody coating process.

This study therefore proves that nanograss has excellent potential for use as a biocompatible material for BioMEMS and biosensors where researchers are trying to perform particle capture and sensing. Many more studies are required with a variety of other bioparticles to prove that nanograss will indeed serve well at capturing and sensing them.

CHAPTER 7. CONCLUSION AND FUTURE WORK RECOMMENDATIONS

7.1 Conclusion

The aim of this thesis was to investigate the capture and sensing ability of BioMEMS material—nanograss—for biomedical applications as a biosensor. This study showed how to fabricate such devices efficiently at low cost. A biocompatible interface can be achieved with post-processing, after fabricating the nanograss itself. Experiment setup and impedance measurement procedure were illustrated in this study to develop a nanograss-based impedance biosensor for a new application of sensitive and rapid detection of bioparticles. The results demonstrated that the IDA microelectrode based impedance sensor was able to detect fluorescent beads at a low concentration, and bulk electrolyte solution as well.

This study compared the impedance spectroscopy of fluorescent beads in PBS with DI water in PBS (same dilution ratio), to rule out the effect of DI water coming in with the fluorescent beads from the company. The results also suggested that nanograss is capable of capturing such particles and sensing them via an impedimetric method. This capability was determined by integrating the capture module and sensing module onto a single device.

7.2 Recommendations for Future Work

Although, this study looked at the capture and sensing ability of a nanograss embedded microfluidic device, no virus or bacteria experiment was performed. Prior to declaring nanograss as a biomaterial for an impedimetric sensor, it will be extremely important to check the capture efficiency and sensitivity of such device on different types of bioparticles. Studies have shown that cell sensing can be done quite well with the impedimetric method, but virus and bacteria need to be double-checked. Also, it will be important to optimize the fabrication process of nanograss itself, to make it possible to control the morphology and etching profile of nanograss. Until then, nanograss can be considered a promising structure for biosensing.

REFERENCES

[1] UNAIDS and WHO, AIDS Epidemic Update, 2009, [Online] http://data.unaids.org/pub/Report/2009/jc1700_epi_update_2009_en.pdf.

[2] Phillips, C. Lee, J. Elford, G. Janossy, A. Timms, M. Bofill and P. Kernoff, "Serial CD4 lymphocyte counts and development of AIDS," *Lancet*, 1991, vol. 337, no. 8738, pp. 389-392.

[3] M. Kitahata, S. Gange, A. Abraham, B. Merriman, M. Saag, A. Justice, R. Hogg, S. Deeks, J. Eron, J. Brooks, S. Rourke, M. Gill, R. Bosch, J. Martin, M. Klein, L. Jacobson, B. Rodriguez, T. Sterling, G. Kirk, S. Napravnik, A. Rachlis, L. Calzavara, M. Horgerg, M. Silverberg, K. Gebo, J. Goedert, C. Benson, A. Collier, S. Van Rompaey, H. Crane, R. McKaig, B. Lau, A. Freeman and R. Moore, "Effect of early versus deferred antiretroviral therapy for HIV on survival," *N. Engl. J. Med*., 2009, vol. 360, no. 18, pp. 1815-1826.

[4] V. Greengrass, M. Plate, P. Steele, J. Denholm, C. Cherry, L. Morris, A. Hearps, and S. Crowe, "Evaluation of the Cavidi ExaVir load assay (Version 3) for plasma human immunodeficiency virus type 1 load monitoring," *J. Clin. Microbiol.*, 2009, vol. 47, no. 9, pp. 3011–3013.

[5] P. Takhistov, "Electrochemical synthesis and impedance characterization of nano-patterned biosensor substrate," *Biosens. Bioelectron*., 2004, vol. 19, no. 11, pp. 1445–1456.

[6] De la Escosura-Muñiz, and A. Merkoçi, "A nanochannel/nanoparticle-basedfiltering and sensing platform for direct detection of a cancer biomarker in blood," *Small*, 2011, vol. 7, no. 5, pp. 675–682.

[7] G. Koh, S. Agarwal, P.S. Cheow, and C.S. Toh, "Development of a membrane-based electrochemical immunosensor," *Electrochimca Acta*, 2007, vol. 53, no. 2, pp. 3803–3810.

[8] B.T.T. Nguyen, G. Koh, H.S. Lim, A.J.S. Chua, M.M.L. Ng, and C.S. Toh, "Membrane-based electrochemical nanobiosensor for the detection of virus," *Anal. Chem.*, 2009, vol. 81, no. 17, pp. 7226–7234.

[9] K.C. Lin, V. Kunduru, M. Bothara, K. Rege, S. Prasad, and B.L. Ramakrishna, "Biogenic nanoporous silica-based sensor for enhanced electrochemical detection of cardio-vascular biomarkers proteins," *Biosens. Bioelectron*., 2010, vol. 25, no. 10, pp. 2336–2342.

[10] F. Tan, P.H.M. Leung, Z.B. Liu, Y. Zhang, L.D. Xiao, W.W. Ye, X. Zhang, L. Yi, and M. Yang, "A PDMS microfluidic impedance immunosensor for E. coli O157:H7 and Staphylo-coccus aureus detection via antibody-immobilized nanoporous membrane," *Sens.Actuator B Chem*, 2011, vol. 159, no. 1, pp. 328-335.

[11] J. Wang, K. S. Carmon, L. A. Luck, and I. I. Suni, "Electrochemical impedance biosensor for glucose detection utilizing a periplasmic E. coli receptor protein," *Electrochemical and Solid-State Letters,* 2005, vol. 8, no. 8, pp. 61-64.

[12] N. Watkins, D. Irimia, M. Toner, and R. Bashir, "On a chip," *IEEE Pulse*, Nov.-Dec. 2011, pp. 19-27.

[13] C. D. Chin, V. Linder, and S. K. Sia, "Commercialization of microfluidic point-of-care diagnostic devices," *Lab Chip*, 2012, vol. 12, no. 2, pp. 2118-2134.

[14] G. J. Kost, *Principles and Practices of Point-of-Care Testing*, Lippincott Williams & Wilkins, Philadelphia, 2002.

[15] J. Bartlett and D. Stirling, "A short history of the polymerase chain reaction," *Methods Mol. Biol.*, 2003, vol. 226, pp. 3–6.

[16] R. Saiki, S. Scharf, F. Faloona, K. Mullis, G. Horn, H. Erlich, and N. Arnheim, "Enzymatic amplification of beta-globin genomic sequences and restriction site analysis for diagnosis of sickle cell anemia," *Science*, 1985, vol. 230, no. 4732, pp. 1350–1354.

[17] M. J. Fulwyler, "Electronic separation of biological cells by volume," *Science* 12 Nov. 1965, vol. 150, no. 3698, pp. 910-911.

[18] S. Bae, H. Park, J. Oh, S.-Y. Yoon, D. Park, I. Choi, J. Kim, J. Oh, D. Hur, C. Chung, J. Chang, J. Robinson, and C. Lim, "Absolute CD4+ cell count using a plastic microchip and a microscopic cell counter," *Cytometry B Clin Cytom.*, 2009, vol. 76, no. 5, pp. 345-353.

[19] W. Rodriguez, N. Christodoulides, P. Floriano, S. Graham, S. Mohanty, M. Dixon, M. Hsiang, T. Peter, S. Zavahir, I. Thior, D. Romanovicz, B. Bernard, A. P. Goodey, B. D. Walker, and J. McDevitt, "A microchip CD4 counting method for HIV monitoring in resource-poor settings," 2005, vol. 2, no. 7, pp. 82.

[20] J. Jokerst, P. Floriano, N. Christodoulides, G. Simmons and J. McDevitt, "Integration of semiconductor quantum dots into nano-bio-chip systems for enumeration of CD4+ T cell counts at the point-of-need," *Lab Chip*, 2008, vol. 8, no. 12, pp. 2079-2090.

[21] A. A. Adams, P. I. Okagbare, J. Feng, M. L. Hupert, D. Patterson, J. Gottert, R. L. McCarley, D. Nikitopoulos, M. C. Murphy, and S. A. Soper, "Highly efficient circulating tumor cell isolation from whole blood and label-free enumeration using polymer-based microfluidics with an integrated conductivity sensor," *J. Am. Chem. Soc.*, 2008, vol. 130, no. 27, pp. 8633–8641.

[22] T. Li, Q. Fan, T. Liu, X. Zhu, J. Zhao, and G. Li, "Detection of breast cancer cells specially and accurately by an electrochemical method," *Biosens. Bioelectron.*, 2010, vol. 25, no. 12, pp. 2686–2689.

[23] R. de la Rica, S. Thompson, A. Baldi, C. Fernandez-Sanchez, C. M. Drain, and H. Matsui, "Label-free cancer cell detection with impedimetric transducers," *Anal. Chem.*, 2009, vol. 81, no. 24, pp. 10167–10171.

[24] A. R. A. Rahman, C. M. Lo, and S. Bhansali, "A detailed model for high-frequency impedance characterization of ovarian cancer epithelial cell layer using ECIS electrodes," *IEEE Trans. Biomed. Eng.*, 2009, vol. 56, no. 2, pp. 485–492.

[25] A. Rahman and A. Guiseppi-Elie, "Design considerations in the development and application of microdisc electrode arrays (MDEAs) for implantable biosensors," *Biomed. Microdevices*, 2009, vol. 11, no. 3, pp. 701–710.

[26] T. J. Davies and R. G. Compton, "The cyclic and linear sweep voltammetry of regular arrays of microdisc electrodes: Fitting of experimental data," *J. Electroanal. Chem.*, 2005, vol. 585, no. 1, pp. 63–82.

[27] S. Arya, K. Lee, D. Dahalan, and A. Rahman, "Breast tumor cell detection at single cell resolution using an electrochemical impedance technique," *Lab Chip*, 2012, vol. 12, no. 13, pp. 2362–2368.

[28] X. Jiang and M. G. Spencer, "Electrochemical impedance biosensor with electrode pixels for precise counting of CD4+ cells: a microchip for quantitative diagnosis of HIV infection status of AIDS patients," *Biosens. Bioelectron.*, 2010, vol. 25, no. 7, pp. 1622–1628.

[29] B. Lakshmi, P. Dorhout, and C. Martin, "Sol-Gel template synthesis of semiconductor nanostructures," *Chem. Mater.*, 1997, vol. 9, no. 3, pp. 857–862.

[30] H. Masuda and K. Fukuda, "Ordered metal nanohole arrays made by a two-step replication of honeycomb structures of anodic alumina," *Science*, 1995, vol. 268, no. 5216, pp. 1466–1468.

[31] B. Nguyen, G. Koh, H. Lim, A. Chua, M. Ng, and C. Toh, "Membrane-based electrochemical nanobiosensor for the detection of virus," *Anal. Chem.*, 2009, vol. 81, no. 17, pp. 7226–7234.

[32] S. Li, J. Li, K. Wang, C. Wang, J. Xu, H. Chen, X. Xia, Q. Huo, "Membrane-based electrochemical nanobiosensor for the detection of virus," *ACS Nano*, 2010 vol. 4, no. 11, pp. 6417–6424.

[33] N. Kam, M. O'Connell, J. Wisdom, H. Dai, "Carbon nanotubes as multifunctional biological transporters and near-infrared agents for selective cancer cell destruction," *Proc. Natl. Acad. Sci.*, 2005, vol. 102, no. 33, pp. 11600–11605.

[34] B. Dorvel, B. Reddy, J. Go, C. Guevara, E. Salm, M. Alam, and R. Bashir, "Silicon nanowires with high-k hafnium oxide dielectrics for sensitive detection of small nucleic acid oligomers," *ACS Nano*, 2012, vol. 6, no.7, pp. 6150-6164.

[35] M. Bothara, V. Venkatraman, R. Reddy, T. Barrett, J. Carruthers, and S. Prasad, "Nanomonitors: electrical immunoassays for protein biomarker profiling," *Nanomedicine (Lond)*, 2008, vol. 3, no. 4, pp. 423–436.

[36] G. Chen, F. Fachin, E. Colombini, B. Wardle, and M. Toner, "Nanoporous micro-element arrays for particle interception in microfluidic cell separation," *Lab Chip*, 2012, vol. 12, no. 17, pp. 3159-3167.

[37] Y. Kim, S. Moon, D. Kuritzkes, and U. Demirci, "Quantum dot-based HIV capture and imaging in a microfluidic channel," *Biosensors and Bioelectronics*, 2009, vol. 25, no. 1, pp. 253–258.

[38] D. Akin, H. Li, and R. Bashir, "Real-time virus trapping and fluorescent imaging in microfluidic devices," *Nano Letters*, 2004, vol. 4, no. 2, pp. 257-259.

[39] K. Park, D. Akin, and R. Bashir, "Electrical capture and lysis of vaccinia virus particles using silicon nano-scale probe array," *Biomed. Microdevices*, 2007, vol. 9, no. 6, pp. 877–883.

[40] H. Jansen, M. de Boer, R. Legtenberg and M. Elwenspoek, "The black silicon method: a universal method for determining the parameter setting of a fluorine-based reactive ion etcher in deep silicon trench etching with profile control," *J. Micromech. Microeng.*, 1995, vol. 5, pp. 115-120.

[41] J. Karttunen, J. Kiihamäki, and S. Franssila, "Loading effects in deep silicon etching," *Proceedings of SPIE*, 2000, vol. 4174, pp. 90–97.

[42] C. Mogab, "The loading effect in plasma etching," *J. Electrochem. Soc.*, 1977, vol. 124, no. 8, pp. 1262-1268l.

[43] I. Levchenko, U. Cvelbar, and K. Ostrikov, "Kinetics of the initial stage of silicon surface oxidation: deal; grove or surface nucleation," *Appl. Phys. Lett.*, 2009, vol. 95, no. 2, pp. 21502–21503.

[44] H. Oh, K. Jang, and C. Chi, "Impedance characteristics of oxide layers on aluminium," *Bull. Korean Chem. Soc.*, 1999, vol. 20, no. 11, pp. 1340-1344.

[45] M. Takahashi, T. Nagao, Y. Imazeki, K. Matsuzaki, and H. Minamitani, "Fluorescence image analysis for quantification of active oxygen induced by photochemical reaction," presented at 23rd Annual International Conference of the IEEE Engineering in Medicine and Biology Society, Istanbul, Turkey, 2011.

[46] C. Mathilde and Q. David, "On water repellency," *Soft Matter*, 2005, vol. 1, pp. 55-61.

[47] R. N. Wenzel, "Resistance of solid surfaces to wetting by water," *Ind. Eng. Chem.*, 1936, vol. 28, no. 8, pp. 988-994.

[48] A. Cassie and S. Baxter, "Wettability of porous surfaces," *Trans. Faraday Soc.*, 1944, vol. 40, pp. 546-551.

[49] L. Feng, Y. Zhang, J. Xi, Y. Zhu, N. Wang, F. Xia, and L. Jiang, "Petal effect: a superhydrophobic state with high adhesive force," *Langmuir*, 2008, vol. 24, no. 8, pp. 4114-4119.

[50] S. Herminghaus, "Roughness-induced non-wetting," *Europhys. Lett.*, 2000, vol. 52, no.2, pp. 165-170.

[51] E. Bormashenko, T. Stein, G. Whyman, Y. Bormashenko, and R. Pogreb, "Shape, vibrations, and effective surface tension of water marbles," *Langmuir*, 2006, vol. 22, no. 24, pp. 9982–9985.

[52] A. Marmur, "Wetting on hydrophobic rough aurfaces: to be heterogeneous or not to be?" *Langmuir*, 2003, vol. 19 no. 20, pp. 8343–8348.

[53] N. Watkins, S. Sridhar, X. Cheng, M. Toner, W. Rodriguez, and R. Bashir, "A microfabricated electrical differential counter for the selective enumeration of CD4+ T lymphocytes," *Lab Chip*, 2011, vol. 11, no. 8, pp.1437-1447.

[54] M. Sha, S. Penn, G. Freeman and W. Doering, "Detection of Human Viral RNA Via a Combined Fluorescence and SERS Molecular Beacon Assay," *Nanobiotechnology*, 2007, vol. 3, no. 1, pp. 23-30.

[55] A. Michaels, M. Nirmal, and L. Brus, "Surface enhanced Raman spectroscopy of individual Rhodamine 6G molecules on large Ag nanocrystals," *J. Am. Chem. Soc.*, 1999, vol. 121, no. 43, pp. 9932-9939.

[56] C. Ruan, L. Yang, Y. Li, "Immunobiosensor chips for detection of E. coil O157:H7 using electrochemical impedance spectroscopy," *Anal. Chem.*, 2002, vol. 74, no. 18, pp. 4814-4820.

[57] A. Bard and L. Faulkner, *Electrochemical Methods: Fundamentals and Applications*, Wiley, New York, 1980.

[58] L. Yang and Y. Li, "AFM and impedance spectroscopy characterization of the immobilization of antibodies on indium-tin oxide electrode through self-assembled monolayer of epoxysilane and their capture of Escherichia coli O157:H7," *Biosens. Bioelectron.*, 2005, vol. 20, no. 7, pp. 1407-1416.

[59] H. Tang, J. Chen, L. Nie, Y. Kuang, and S. Yao, "A label-free electrochemical immunoassay for carcinoembryonic antigen (CEA) based on gold nanoparticles (AuNPs) and nonconductive polymer film," *Biosens. Bioelectron.*, 2007, vol. 22, no. 6, pp. 1061-1067.

[60] J. Randles, "Kinetics of rapid electrode reactions," Discussions of the Faraday Society 1: 11, 1947.